1   **Cryo-EM structures reveal multiple stages of bacterial outer membrane protein folding**

2

3   Matthew Thomas Doyle[#,1], John R. Jimah[#,2], Jenny E. Hinshaw*[,2], Harris D. Bernstein*[,1]

4

5   [#]Equal Contribution

6

7   *Corresponding Authors:

8   Harris D. Bernstein. Email: harris_bernstein@nih.gov

9   Jenny E. Hinshaw. Email: jenny.hinshaw@nih.gov

10

11   Departments / Addresses:

12   [1]Genetics and Biochemistry Branch, National Institute of Diabetes and Digestive and Kidney

13   Diseases, National Institutes of Health, Bethesda, MD 20892 USA

14   [2]Laboratory of Cell and Molecular Biology, National Institute of Diabetes and Digestive and

15   Kidney Diseases, National Institutes of Health, Bethesda, MD 20892 USA

16

17

SUMMARY

Transmembrane β-barrel proteins are folded into the outer membrane (OM) of Gram-negative bacteria by the β-barrel assembly machine (BAM) via an unexplained process that occurs without known external energy sources. Here we used single-particle cryo-EM to visualize the folding dynamics of a model β-barrel protein (EspP) by BAM. We found that BAM binds the highly conserved "β-signal" motif of EspP to correctly orient β-strands in the OM during folding. We also found that the folding of EspP proceeds via remarkable "hybrid-barrel" intermediates in which membrane integrated β-sheets are attached to the essential BAM subunit, BamA. The structures show an unprecedented deflection of the membrane surrounding the EspP intermediates and suggest that β-sheets progressively fold towards BamA to form a β-barrel. Along with *in vivo* experiments that tracked β-barrel folding while the OM tension was modified, our results support a model in which BAM harnesses OM elasticity to accelerate β-barrel folding.

KEYWORDS

membrane protein folding, membrane dynamics, outer membrane protein, BAM, β-barrel.

INTRODUCTION

The insertion and folding of integral membrane proteins involves fundamentally complex

processes that require management of hydrophobic and hydrophilic interfaces during

intermediate steps to arrive at a topologically correct and functional structure. The biogenesis of

proteins located in the outer membrane (OM) of Gram-negative bacteria and organelles of

bacterial origin that span the membrane via a unique "β-barrel" structure is especially enigmatic,

in part because they rapidly insert into the OM in the absence of known external energy sources

(Horne et al., 2020; Tomasek and Kahne, 2021). For unknown reasons, almost all bacterial outer

membrane proteins (OMPs) contain a transmembrane β-barrel. Although they can vary greatly in

size (8 – 36 β-strands) and can be linked to soluble domains, transmembrane β-barrels generally

conform to common architectural rules (Gruss et al., 2013; Horne et al., 2020; Lauber et al.,

2018; Schulz, 2000). OMP β-barrels are tilted amphipathic anti-parallel β-sheets that are closed

by tight hydrogen-bonding between the first and last β-strands (the "β-seam") into super-stable

cylinders (Horne et al., 2020; Schulz, 2000). Transmembrane β-barrels are also stabilized in the

OM by parallel "girdles" of membrane-facing aromatic residues (Schulz, 2000). The majority

(77%) of β-barrels also have a highly conserved C-terminal motif called the "β-signal" that

contains an essential terminal phenylalanine residue of unknown function (Struyve et al., 1991;

Wang et al., 2021). In bacteria, the assembly (folding and integration) of β-barrels is catalyzed

by a heterooligomer called the β-barrel assembly machine (BAM) (Heinz and Lithgow, 2014;

Heinz et al., 2015; Wu et al., 2005). In *E. coli*, BAM is composed of an essential subunit

(BamA), and four lipoproteins (BamBCDE) (Wu et al., 2005). BamA is conserved in all Gram-

negative bacteria, and essential homologs are also found in mitochondria and chloroplasts (Heinz

and Lithgow, 2014; Kozjak et al., 2003; Patel et al., 2008; Voulhoux et al., 2003). BamD is

58   likewise highly conserved throughout bacteria but is conditionally essential (Anwari et al., 2012;

59   Hart et al., 2020; Hart and Silhavy, 2020). BamA is itself an OMP that contains a C-terminal β-

60   barrel domain and five soluble N-terminal polypeptide transport-associated (POTRA) domains

61   that bind the lipoproteins (Gu et al., 2016; Han et al., 2016; Iadanza et al., 2016).

62   The structural dynamics that occur as OMPs transition from an incompletely folded state

63   to a fully folded β-barrel remain unclear. However, available evidence suggests that OMP β-

64   signals may be recognized by BAM and that the unusual conformational malleability of BAM

65   (particularly BamA) may facilitate the folding process (Doerner and Sousa, 2017; Doyle and

66   Bernstein, 2019; Hagan et al., 2015; Iadanza et al., 2016; Kaur et al., 2021; Lundquist et al.,

67   2018; Noinaj et al., 2014; Tomasek et al., 2020; White et al., 2021). Interestingly, BamA does

68   not contain a canonical β-signal at its C-terminus, but instead has a "kinked" structure that causes

69   its terminal residues to move dynamically and generate a unique unstable β-seam (that forms

70   hydrogen-bonds poorly) (Lundquist et al., 2018; Noinaj et al., 2013). BamA can also adopt either

71   inward-open or outward-open conformational states (in which the BamA β-barrel lumen is open

72   to the inside of the cell but closed on the surface or *vice versa*) that coincide with the opening

73   and closing of its β-seam (Gu et al., 2016). Experiments in which the BamA β-seam was tethered

74   closed by disulfide bonds indicates that the opening and/or closing of BamA is required for

75   efficient β-barrel folding (Gu et al., 2016; Iadanza et al., 2016; Noinaj et al., 2014). To explain

76   the requirement for BamA β-seam opening, we recently performed an *in vivo* crosslinking study

77   that captured a snapshot of the folding process in which the β-signal strand of an incompletely

78   folded β-barrel was fully paired with BamA β-strand 1 (β1) via an antiparallel inter-strand

79   interface to form a remarkable "hybrid-barrel" intermediate folding state (Doyle and Bernstein,

80   2019). In that study, the opposing interface between the C-terminus of BamA and the N-terminus

81   of the β-barrel substrate was extremely dynamic, which suggests the presence of multiple

82   transition states during the assembly process (Doyle and Bernstein, 2019). A 4 Å resolution cryo-

83   electron microscopy (cryo-EM) structure of BAM engaged during the folding of an assembly

84   deficient BamA deletion mutant (BamA$_{\Delta L1}$) in detergent micelles also showed BamAβ1 bound to

85   the C-terminus of BamA$_{\Delta L1}$ to form a late-stage hybrid-barrel intermediate (Tomasek et al.,

86   2020). Although the structure might depict a similar stage of β-barrel folding, the BAM-

87   BamA$_{\Delta L1}$ interface is twisted and results in a "W-shaped" structure that is not fully hybridized

88   (Tomasek et al., 2020). Due to its non-canonical final structure, it is likely that this transition

89   state is specific to the assembly of BamA and does not occur during the folding of typical OMPs.

90   Moreover, the BAM-BamA$_{\Delta L1}$ structure did not show how BAM recognizes the terminal

91   phenylalanine in β-signals or reveal the dynamics of the folding process that results in the late

92   hybrid-barrel state.

93   Mostly because the reconstitution of the native OM *in vitro* remains a significant

94   technical challenge, the role of the membrane itself in OMP folding has often been neglected.

95   Unlike other biological membranes, the bacterial OM is an asymmetric bilayer that is composed

96   of a unique glycolipid known as lipopolysaccharide (LPS) in the outer leaflet and phospholipids

97   in the inner leaflet (Horne et al., 2020). The concentration of OMPs within the OM is also

98   extremely high and has been estimated to account for the majority of the OM volume (Horne et

99   al., 2020; Jaroslawski et al., 2009). Because the interactions between densely packed β-barrels

100   and LPS molecules results in a rigid structure in which protein diffusion is low (Rassam et al.,

101   2015; Rojas et al., 2018; Ursell et al., 2012), the mechanism by which β-barrels are folded into

102   the OM is even more puzzling. A recent study showed that the BAM lipoproteins can alter

103   membrane fluidity (albeit in synthetic bilayers) and thereby potentially facilitate β-barrel

104   integration (White et al., 2021). Intriguing molecular dynamics simulations have also raised the

105   possibility that the unique 'wedge-shaped" aromatic girdles of the BamA β-barrel might thin the

106   OM to reduce the energy required for assembly (Liu and Gumbart, 2020; Noinaj et al., 2013).

107   Here, we examined the folding of a model *E. coli* O157:H7 OMP (EspP) that contains a

108   stably closed β-seam, an average sized β-barrel (12 β-strands), and a canonical β-signal (Barnard

109   et al., 2007; Franklin et al., 2018; Wang et al., 2021). By using single-particle cryo-EM to

110   analyze an assembly-arrested form of the protein associated with BAM in native-nanodiscs that

111   contain components directly extracted from the bacterial OM (unlike previous structural studies

112   that analyzed BAM in detergent or nanodiscs with synthetic phospholipid bilayers), we were able

113   to visualize multiple intermediate stages of β-barrel folding. Unlike BamA$_{\Delta L1}$, EspP forms an

114   intermediate structure in which its conserved β-signal is fully hybridized with BamA to form a

115   "B-shaped" hybrid-barrel. The critical phenylalanine residue in the EspP β-signal is positioned

116   on BAM within an unusual binding pocket that interfaces with the OM to correctly orient the

117   new OMP during folding. We also obtained direct evidence that BAM alters the structure of the

118   OM via membrane thinning and interfacial LPS / lipid stabilization. Remarkably, in some of the

119   intermediate hybrid-barrel structures, the OM around the folding EspP β-barrel was deflected at

120   an angle relative to the plane of the OM around BamA. This phenomenon is unlike any known

121   membrane-bending process (Prinz and Hinshaw, 2009). Our structural data, combined with the

122   results of *in vivo* experiments in which β-barrel assembly was monitored during transient

123   modulation of OM tension, led us to a completely novel model in which BAM utilizes the

124   intrinsic structure of β-barrels and the mechanical properties of the OM itself to accelerate the

125   final stages of OMP folding.

126 **RESULTS**

127 **Structure of BAM folding a β-barrel substrate in native OM nanodiscs**

128 To isolate an active form of BAM that is engaged in catalyzing the folding of a new β-barrel, we

129 utilized a derivative of EspP ([MBP-76]EspP) whose assembly is arrested at a late stage while it is

130 still bound to BAM (Doyle and Bernstein, 2019, 2021). EspP is a member of the autotransporter

131 family of OMPs that consist of a C-terminal β-barrel and an N-terminal extracellular

132 ("passenger") domain that is translocated across the OM by BamA (Doyle and Bernstein, 2021;

133 Rossiter et al., 2011). To construct [MBP-76]EspP, we replaced most of the passenger domain with

134 maltose binding protein (MBP), a protein that folds rapidly in the periplasm (the space between

135 the inner membrane and OM) and, consequently, prevents translocation due to the size

136 constraints of the channel (Doyle and Bernstein, 2019). Because translocation must be completed

137 before BamA releases a fully folded EspP β-barrel (Ieva and Bernstein, 2009; Ieva et al., 2011),

138 [MBP-76]EspP remains bound to BamA in a hybrid-barrel state in which the β-signal is fully

139 hybridized to BamAβ1 (Doyle and Bernstein, 2019). Importantly, BAM-[MBP-76]EspP co-

140 complexes represent *bona fide* folding intermediates because β-barrel folding can be completed

141 when the MBP containing portion of [MBP-76]EspP is released by proteolysis (Doyle and Bernstein,

142 2019, 2021). To increase stability during purification, we used an *E. coli* strain transformed with

143 plasmids expressing [His]BamA$_{S425C}$BCDE and [MBP-76]EspP$_{S1299C}$ and generated a disulfide-tether

144 between two residues in BamAβ1 and the EspP β-signal that were previously shown to be

145 proximal during the natural hybrid-barrel assembly step *in vivo* (Doyle and Bernstein, 2019). To

146 more faithfully reconstitute an OM environment than previous structural studies on BAM (or

147 other OMPs), we used a detergent-free system involving styrene–maleic acid (SMA) copolymers

148 to directly solubilize and isolate BAM-[MBP-76]EspP co-complexes into native nanodiscs. Based on

149   structural studies on α-helical membrane proteins, our BAM-$^{MBP-76}$EspP OM-nanodiscs likely

150   contain locally derived phospholipids and LPS (Lee et al., 2016; Sun et al., 2018). Purified

151   BAM-$^{MBP-76}$EspP OM-nanodiscs contained lipoproteins in the correct stoichiometry (Figure 1A).

152   The BamA-$^{MBP-76}$EspP hybrid-barrel exhibited an intrinsic feature of β-barrels when examined

153   by SDS-PAGE in that in the absence of heat it was resistant to unfolding by SDS and migrated

154   more rapidly (Doyle and Bernstein, 2019; Noinaj et al., 2015). Furthermore, the rapidly

155   migrating BamA-$^{MBP-76}$EspP hybrid-barrels also ran as diffuse bands (Figure 1A, left lane) that

156   presumably resulted from dynamic interactions between the EspP β-barrel N-terminal strand and

157   BamA C-terminal strands that were previously observed during folding *in vivo* (Doyle and

158   Bernstein, 2019).

159   A high-resolution structure of the purified BAM-$^{MBP-76}$EspP OM-nanodiscs was solved to

160   a global resolution of 3.6 Å by single particle cryo-EM (Figure 1B & Figure S1). The structure

161   revealed BamA in an overall outward-open conformation with BamAβ1 associated with the EspP

162   β-signal to form a hybrid-barrel intermediate folding state (Figure 1B). In this map only four C-

163   terminal β-strands of the actively folding EspP β-barrel were clearly resolved. These β-strands

164   extended into a low-resolution region within the OM-nanodisc that likely represents the

165   remainder of the amphipathic EspP β-barrel creating a border between the membrane and an

166   internal hydrophilic cavity (Figure 1C). The low resolution of the EspP β-barrel N-terminus

167   suggests that this portion of the protein transitions between multiple highly dynamic folding

168   substates, a notion consistent with the previously observed dynamic interface between the EspP

169   β-barrel N-terminus and BamAβ15/16 mentioned above (Doyle and Bernstein, 2019).

170   Comparison of our structure to the BAM-BamA$_{\Delta L1}$ structure (Tomasek and Kahne, 2021)

171   showed striking differences. While the hybridization interface between BAM and the BamA$_{\Delta L1}$

172   mutant is twisted to form a W-shaped hybrid-barrel, the BamA-EspP hybridization interface

173   instead forms a continuous flat β-sheet (Figure 1D). This difference stems from the ability of

174   BamAβ1/2 to flex and tilt in the membrane and suggests a mechanism by which BamA can

175   accommodate the folding and integration of different β-barrel substrates. In the BAM-$^{MBP-76}$EspP

176   structure, BamA POTRA3 and BamB (through its association with POTRA3) are also positioned

177   closer to the membrane (Figure 1D "P3" & Figure S1). Conformational changes localized near

178   the N-terminal α-helices of BamD likewise result in a shift towards the membrane with α-helix 2

179   interfacing with the outer side of the periplasmic turns of the folding EspP β-barrel (Figure 1D &

180   Figure S1). This overall conformation contrasts with the BAM-BamA$_{ΔL1}$ structure in which

181   BamD is positioned beneath the lumen of BamA$_{ΔL1}$. To test whether BamD can interact with the

182   periplasmic turns of EspP during a hybrid-barrel stage of assembly *in vivo*, BAM containing a

183   BamD$_{R49C}$ subunit was co-expressed in *E. coli* with $^{MBP-76}$EspP$_{D1218C}$ (cysteine substitution sites

184   are indicated in Figure 1D) and cells were treated with a thiol-specific disulfide-oxidation

185   catalyst. Consistent with our structure, strong disulfide-crosslinking between $^{MBP-76}$EspP$_{D1218C}$

186   and BamD$_{R49C}$ was observed after chemical oxidation but not in the control strain expressing a

187   wild type (WT) BamD allele (Figure 1E). The observation that crosslinking plateaued at ~40%

188   suggests the presence of additional substates with alternative conformations of EspP relative to

189   BamD (Figure 1E plot & Figure S1). A higher than expected level of spontaneous crosslinking

190   (~10%, Figure 1E, Ox-) also indicated the existence of a stage in which EspP interacts with

191   BamD very stably.

192   Strikingly, in the BAM-$^{MBP-76}$EspP structure we were able to clearly resolve the

193   conserved residues of the canonical β-signal of EspP (Figure 1B & 1F). The terminal EspP β-

194   signal residue (F1300) is oriented over BamAβ1 in a space created by BamA$_{G424}$ that forms a

195   novel structural arrangement reminiscent of stabilizing intra-barrel "mortise-tenon joints"

196   (Figure 1F &1G) (Leyton et al., 2014). BAM interacts with F1300 via BamA T423, G424, F426,

197   and Q446 within an unusual membrane facing hydrophobic pocket (Figure 1F). Nevertheless, the

198   β-signal binding pocket is not totally filled. Presumably this property enables BAM to

199   accommodate the less common subset of OMPs that have β-signals terminated by tryptophan or

200   tyrosine instead of phenylalanine (Struyve et al., 1991; Wang et al., 2021). The conserved β-

201   signal residue at the -3 position of EspP (Y1298) interacts with BamD L124 and is oriented into

202   the membrane plane at a depth corresponding to the aromatic girdles of fully folded canonical β-

203   barrels (Figure 1F). Overall, the structure suggests that BAM binds to β-signals to correctly

204   orient the C-terminal strands of new OMPs into the OM during the folding process. Interestingly,

205   darobactin (a recently discovered BAM inhibitor) (Imai et al., 2019) and the β-signal interact

206   with BamAβ1 in a highly similar way; like EspP F1300, the terminal phenylalanine of the

207   darobactin peptide is positioned over BamA$_{G424}$ (Kaur et al., 2021) (Figure 1G). Therefore, our

208   structure not only provides the structural basis for native OMP β-signal binding by BAM during

209   assembly, but also definitively shows that darobactin is a competitive inhibitor of OMP substrate

210   recognition and thereby helps to explain its bactericidal potency.

211   An important aspect of our study is that by solving the structure of BAM-[MBP-76]EspP

212   within native nanodiscs that harbor local OM lipids captured during solubilization, we can

213   consider the role of the of the OM in OMP assembly. In our BAM-[MBP-76]EspP map, we observed

214   a repetitive pattern of stabilized density circling the BamA β-barrel at the expected location and

215   size of outer leaflet LPS lipid A head groups and clear boundaries that likely represent density

216   for inner leaflet phospholipid headgroups (Figure 2A left & middle). It has been postulated that

217   BamA locally thins the OM to decrease the energetic penalty of OMP integration (Liu and

10

218   Gumbart, 2020; Noinaj et al., 2013). To test this hypothesis, we measured the membrane

219   thickness at positions that had clear and repeatable density proximal to BamA (Figure 2A right &

220   Figure S2). The membrane near the N-terminal half of the BamA β-barrel (~β1 – β7) is ~25 – 26

221   Å in width. This value corresponds closely to the estimated average thickness of the OM (~25 Å)

222   (Wu et al., 2014) and is slightly thicker than the average hydrophobic region of OMPs (~24 Å)

223   (Lomize et al., 2011). Interestingly, the side of the OM-nanodiscs near strands β8 – β13

224   exhibited prominent local thinning to a "pinch-point" (~20 Å) that thickens again near the C-

225   terminal BamA curl. These observed membrane depth patterns perfectly match recent molecular

226   dynamics simulations that predict thickening/thinning patterns around BamA (Liu and Gumbart,

227   2020). The map also suggests even more extreme membrane thinning across strands β14 – 16,

228   but the density does not have clear boundaries for measurement. At the location of the pinch-

229   point we also observed striking density that likely corresponds to a lipid A moiety with a single

230   stabilized acyl chain (the other lipid A acyl chains are presumably dynamic) (Figure 2B). The

231   stabilized acyl chain lies within a groove alongside BamA strands β 11/12 that is created by the

232   lipid-facing residues G631 and A714. Because the membrane thickness and stabilization patterns

233   observed in the high-resolution BAM-[MBP-76]EspP structure were likewise observed in our

234   subsequent independent BAM-[MBP-76]EspP reconstructions (see below and Figure S2), they are

235   likely valid structural features. We speculate that the stabilization of lipid acyl chains on the C-

236   terminal side of BamA is helpful for the process of membrane thinning.

237

238   **The BAM, the OM, and the incoming OMP each undergo major structural transitions**

239   **during β-barrel folding**

11

240   To generate the BAM-$^{MBP-76}$EspP structure described in the preceding section, we started from a

241   pool of ~1.2M high quality particles generated in RELION and obtained the high-resolution map

242   after rounds of heterogenous refinement in cryoSPARC. Although our map had a higher global

243   resolution than the previously solved BAM-BamA$_{\Delta L1}$ structure, the local resolution was poor in

244   the area corresponding to the N-terminal portion of the EspP β-barrel and low for BamA P3 /

245   BamB and the N-terminus of BamD (Figure 3A) presumably due to significant dynamicity in

246   these regions. During processing we noticed specific low-resolution classes that appeared to have

247   alternate conformations in these areas and wondered whether a more conservative processing

248   strategy could improve the local resolution, albeit at the expense of global resolution. To that

249   end, we reprocessed the entire ~1.2M particle pool in RELION into 6 classes and then separately

250   processed each class in cryoSPARC yielding reconstructions with global resolutions between 4.2

251   – 4.5 Å (Figure 3B & Figure S3). The conformation of the BamA β-barrel is essentially identical

252   in all of the structures (Figure 3C). Classes 3, 4 and 6 are similar to the original high-resolution

253   structure but contained slight changes in the position of BamB and the N-terminus of BamD. The

254   density of BamB is poor in class 2 (although it is visible at lower thresholds) presumably because

255   it is highly dynamic (Figure 3B). Indeed, between all the classes the largest overall BAM

256   conformational changes were in the positioning of BamB (Figure 3C & Video S1). Classes 1 and

257   5 represent conformational extremes in which the BamA POTRA domains and BamD move

258   closer or farther away from each other and, concomitantly, BamA P3 moves towards or away

259   from the membrane (Figure 3D). Consequently, this results in very significant changes in BamB

260   positioning (Figure 3D). Together, these reconstructions show that BAM periplasmic

261   components undergo large conformational changes during the late stages of OMP folding that

262   mimic the structural heterogeneity observed in the periplasmic subunits even in apo-BAM

263   (Iadanza et al., 2020).

264   The simple classification approach did not improve the maps in the region corresponding

265   to the folding EspP β-barrel. To better resolve the intermediate folding states of EspP, we

266   subtracted the signals for BamB, BamA P3, and the BamD N-terminus from the original ~1.2M

267   particle pool and conducted focused 3D classification and refinement on the remaining complex.

268   We reasoned that removing these dominant sources of structural heterogeneity would allow

269   better alignment of the conformational substates of the EspP β-barrel N-terminus during the

270   hybrid-barrel stage that were predicted from our earlier experiments *in vivo* (Doyle and

271   Bernstein, 2019). Consistent with our hypothesis, we were able to generate multiple

272   reconstructions of novel hybrid-barrel substates using this processing strategy (Figure 4 and S3).

273   In one structure that we designate the "open-sheet" (OS)-state (Figure 4A), the EspP β-barrel is

274   observed as a remarkable membrane-integrated open β-sheet with its C-terminus hybridized to

275   BamA. In this state the OM-nanodisc is deflected around the EspP transmembrane β-sheet at an

276   angle that results in a mismatch of the membrane plane around BamA (Figure 4A). In the

277   "intermediate-open" (IO)-state (Figure 4B), the reconstructed BAM components are essentially

278   identical to the OS-state with both structures showing BamA in an outward-open conformation.

279   However, compared to the OS-state, in the IO-state the EspP transmembrane β-sheet is folded

280   closer to BamA and the observed membrane deflection is less extreme. In a third structure that

281   we call the "barrelized/continuous-open" (B/CO)-state, we observed a "B-shaped" BamA-EspP

282   hybrid-barrel but, unlike the other states, no obvious membrane deflection (Figure 4C). This state

283   presumably represents a very late stage of EspP assembly in which the β-barrel structure is

284   nearly complete. In the B/CO-state, BAM is observed in a totally novel conformation in which

13

285   the C-terminal half of the BamA β-barrel is expanded away from the N-terminus and

286   repositioned higher in the membrane plane so that its surface loops (including L4, 6, and 7) are

287   shifted away from the EspP β-barrel (Figure 4D). The result is a BamA structure reminiscent of

288   outward-open states but with an opening that creates a continuous channel through the OM-

289   nanodisc (Figure 4D). This structure may represent a stage prior to the release of the EspP β-

290   barrel that we have recently observed *in vivo* in which the BamA β-barrel facilitates secretion of

291   the EspP passenger domain (Doyle and Bernstein, 2021).

292

293   **Antagonism between the intrinsic structure of OMPs and OM tension drives late folding**

294   Although we cannot definitively order the three hybrid-barrel substates in a temporal sequence

295   because they are derived from the same sample, a simple interpretation of the data is that the OS-

296   state represents an early stage of folding following the membrane integration of the EspP β-

297   sheet, the IO-state represents a slightly later stage in which the EspP β-sheet folds towards BamA

298   (Figure 4E), and the B/CO-state represents a relatively late stage in which the β-sheet folds into a

299   barrel-like structure (see Video S2). It is notable that the changes in EspP folding between OS

300   and IO states were not associated with major structural changes in BamA. Furthermore, the

301   extreme nature of the expanded EspP β-sheet and membrane deflections in the OS and IO-states

302   were very surprising and warranted an explanation that places these states in the context of

303   folding within the native OM.

304   To rationalize our findings, we conceptualized a new model of the late stages of OMP

305   assembly by considering the intrinsic structure of transmembrane β-barrels and the rigidity of the

306   OM. OMP β-strands are tilted by ~45° from the barrel-axis (Schulz, 2000) and, due to the

307   presence of aromatic girdles and other membrane-facing hydrophobic residues in β-barrel

308   transmembrane β-sheets, fully folded OMPs are often slightly tilted in the OM (Lomize et al.,

309   2012). We calculated the membrane orientations of solved *E. coli* β-barrels and then illustrated

310   them as open β-sheets while maintaining their β-signals in their calculated positions relative to

311   the OM plane (Figure 5A right, Figure S4A). The result is a mismatch in which the N-terminal

312   transmembrane β-strands would not reside in the normal OM plane but would instead deflect the

313   membrane. Consistent with this hypothetical scenario, the OS and IO-state structures capture

314   EspP as an incompletely-folded open β-sheet at an angle relative to the normal OM plane

315   (Figures 4A, 4B, 5B and S4B). Indeed, in all our structures we observe BamA bound to the EspP

316   β-signal at an even higher angle than the β-signal is situated in after EspP is completely folded

317   (~64.6° vs. 58°, Figure 5A, 5B, & Figure S4B). Furthermore, the difference between the angle of

318   the β-signal of some OMPs when bound to BamA as an open β-sheet versus the fully folded

319   form may be even greater (Figure S4A, see PgaA). The outward-open BamA conformation

320   might therefore create a highly antagonistic scenario between the normal OM plane and the

321   intrinsic structure of incompletely folded β-barrels that deflects the membrane (Figure 4A, 4B,

322   5B). This scenario, however, should be considered in light of the finding that unlike other

323   biological membranes, the OM forms a very rigid structure (stiffer than the peptidoglycan cell

324   wall) due to interactions between LPS molecules, the high OMP density, and the stiffness of

325   OMPs themselves (Horne et al., 2020; Jaroslawski et al., 2009; Lessen et al., 2018; Rojas et al.,

326   2018). Indeed, due to its rigidity, the OM has been observed to function as a 'spring' that

327   undergoes compressive changes during osmotic shock (Rojas et al., 2018). Although stretching

328   and compressive forces appear to be globally equalized across the *E. coli* OM during steady-state

329   growth (Rojas et al., 2018), our model predicts that the intrinsic structure of hybrid-barrel

15

330   deflected β-sheets (Figure 4A, 4B) would be countered by the intrinsic local tensile forces of the

331   OM to help drive the closure of β-barrels (Figure 5B).

332   To test our model *in vivo*, we expressed [MBP-76]EspP alongside BAM in *E. coli* to create a

333   pool of BamA-[MBP-76]EspP hybrid-barrels in the OM and then subsequently monitored late-stage

334   β-barrel folding kinetics during modification of OM tension via osmotic shock. As mentioned

335   earlier, the assembly of [MBP-76]EspP can be restarted from the hybrid-barrel stage by adding a

336   protease that removes the MBP portion responsible for arresting assembly. Completion of

337   folding can then be assessed by monitoring the auto-catalytic cleavage of the passenger domain

338   that occurs after it is fully secreted and the β-barrel reaches its native conformation (Dautin et al.,

339   2007; Ieva and Bernstein, 2009). Consistent with previous studies (Doyle and Bernstein, 2019,

340   2021), adding proteinase K (PK) to bacteria suspended in isotonic LB medium released ~30 kDa

341   C-terminal EspP fragments from the fusion protein that were rapidly converted into folded ~27

342   kDa β-barrels and a peptide derived from the passenger domain that was not detected (Figure 5C

343   top-left and black curve). However, when bacteria were exchanged into a hypertonic LB medium

344   to relax the OM (Rojas et al., 2018) prior to the addition of PK, the incompletely folded C-

345   terminal EspP fragments accumulated and the rate of their conversion to fully folded β-barrels

346   was significantly reduced (Figure 5C bottom-left and blue curve). Although the β-barrel

347   assembly delay under hypertonic conditions was most notable at 5 min after PK addition, by 20

348   min there was no difference in the level of folded β-barrel between the two conditions (Figure

349   5C). This observation strongly suggests that the delay was due to an energetic effect and that the

350   hypertonic conditions did not simply block completion of β-barrel folding. To directly pinpoint

351   the delay to the period that follows the formation of the hybrid-barrel but that precedes the

352   completion of EspP β-barrel folding, the experiment was repeated using the strain expressing

16

353   ^{His}BamA$_{S425C}$BCDE and $^{MBP-76}$EspP$_{S1299C}$. Samples were treated with PK for 5 min (or mock-

354   treated) and oxidized to promote disulfide-crosslinking as described above. Consistent with

355   previous results (Doyle and Bernstein, 2019), strong crosslinks between BamAβ1 and the $^{MBP-}$

356   ^{76}EspP β-signal were detected in oxidized samples without PK treatment (Figure 5D, lanes 3 and

357   6). In samples that were both oxidized and PK treated, the incompletely folded EspP C-terminal

358   fragments were likewise crosslinked to BamA (Figure 5D, lanes 2 and 5, black arrows). These

359   results confirm that hypertonic conditions do not interfere with the stability of the BamA-$^{MBP-}$

360   ^{76}EspP assembly intermediate and pinpoint the delay to the period following the formation of the

361   hybrid-barrel. Interestingly, EspP C-terminal fragments crosslinked to BamA at a statistically

362   higher level under hypertonic conditions at the 5 min time-point (Figure 5D, graph). This finding

363   suggests that the association of incompletely folded EspP with BamA at the hybrid-barrel stage

364   is prolonged when the OM is relaxed.

365   Finally, our model not only predicts that folding can be slowed by relaxing the OM, but

366   that folding can be accelerated by increasing the OM tension. To test this idea, we repeated the

367   assembly restart experiment again under hypertonic conditions, but 5 min after the addition of

368   PK we exchanged the bacteria into an equivalent solution (control) or a hypotonic solution (to

369   increase OM tension) and continued to monitor EspP β-barrel folding. Consistent with our

370   hypothesis, the EspP C-terminal fragments were converted more rapidly into folded β-barrels

371   when they were exchanged into a hypotonic medium (Figure 5E). The difference constitutes a

372   substantial effect given that only a small fraction of incompletely folded EspP molecules

373   remained to be tracked after the 5 min time-point. Together, these results support a model in

374   which BamA orients OMP substrates at an antagonistic angle to the OM to exploit the intrinsic

375   tension of the OM as a useful driving force to accelerate β-barrel folding (Figure 5B).

DISCUSSION

Although the first transmembrane β-barrel structure was solved in 1990 (Weiss et al., 1990), how they are recognized, folded, and released into the bacterial OM in the absence of any known external energy sources remains poorly understood. In this work we provide structural and biochemical evidence that helps to explain all of these critical stages of OMP assembly. We solved ten distinct cryo-EM structures of BAM bound to EspP, a model OMP that contains conserved features found in most transmembrane β-barrels, that likely illustrate distinct intermediate stages in the folding process. Because the co-complex was purified in native nanodiscs instead of detergent or nanodiscs containing synthetic phospholipid bilayers, we were able to obtain insight into how OM lipids contribute to the β-barrel folding process. With respect to substrate recognition, our structural data reveal an unusual pocket in BAM that binds to the highly conserved C-terminal OMP β-signal motif. During the hybrid-barrel intermediate stage, the terminal aromatic residue interacts with several adjacent BAM residues and is positioned over the space created by $BamA_{G424}$. The interaction resembles G-(F/Y/W)-based inter-strand mortise-tenon joints that are found within most OMPs and that provide structural stability (Leyton et al., 2014). However, the BamA-β-signal interaction constitutes the first observation of an inter-barrel mortise-tenon-like joint. The binding of BAM to the β-signal provides an explanation for the finding that mutations of the terminal aromatic residue cause severe assembly defects and lead to OMP degradation *in vivo* (Gessmann et al., 2014; Lee et al., 2018; Wang et al., 2021). Presumably the mutations reduce the binding affinity of incoming OMPs to BAM, prevent their progression to the hybrid-barrel stage, and result in exposure to periplasmic proteases. Our discovery of this binding site may also enable the design of novel competitive inhibitors of β-signal binding and the further development of lead compounds such as darobactin

18

399   (Imai et al., 2019; Kaur et al., 2021) that act as potent antibiotics against multidrug-resistant

400   Gram-negative pathogens.

401   Our results provide evidence that the EspP C-terminal domain inserts into the OM as a β-

402   sheet and then folds into a β-barrel in multiple steps. The structural data suggest that BAM binds

403   to the β-signal strand of EspP to form a flat hybridization interface and that this hybrid-barrel

404   intermediate passes through several substantially different stages of folding (e.g., OS, IO, and

405   B/CO substates) resulting in a "B-shaped" hybrid-barrel. Ultimately, because the BamAβ1-

406   EspP(β-signal) backbone hydrogen-bond network is weaker than that of the β-seam of fully

407   folded EspP (Figure S4C), this configuration provides an energetically favorable mechanism for

408   the release of the substrate into the lipid bilayer. Furthermore, we identified a substate in which

409   BamA exists in a novel continuous-open conformation coinciding with a more barrel-like EspP

410   structure (the B/CO-state). We recently showed that the unfolded passenger domain of [MBP-

411   76]EspP is secreted through the BamA β-barrel lumen during a hybrid-barrel assembly stage *in*

412   *vivo* (Doyle and Bernstein, 2021). We therefore speculate that the continuous opening in BamA

413   observed in the B/CO-state may constitute a channel for the secretion of autotransporter

414   passenger domains and extracellular segments of other OMPs. Despite the stability of [MBP-

415   76]EspP, we found that the passenger domain is extremely dynamic within the channel *in vivo*

416   (Doyle and Bernstein, 2021), and this dynamicity may explain the lack of passenger domain

417   density within the BamA opening in our reconstructions. Alternatively, the conformational

418   changes observed in the surface loops of BamA in the B/CO-state relative to our other structures

419   (e.g., L4, 6, and 7) may be required for the folding of β-barrels more generally. Indeed, this

420   finding may explain why the function of BAM is strongly inhibited when BamA L4 is bound by

421   the bactericidal antibody fragment Fab1 which presumably prevents this conformational cycling

19

422   (White et al., 2021). It is important to note that none of our reconstructions exhibited the twisted

423   interface that results in a hybrid-barrel with a "W-shaped" cross-section observed in the BAM-

424   BamA$_{\Delta L1}$ structure (Tomasek et al., 2020). Besides lacking a canonical C-terminal β-signal, the

425   BamA$_{\Delta L1}$ β-barrel substrate has unique features such as an unstable β-seam, extreme structural

426   dynamism, and a kinked C-terminus that likely causes the twisted hybridization interface

427   observed during its assembly (Doerner and Sousa, 2017; Gu et al., 2016; Iadanza et al., 2016;

428   Lundquist et al., 2018; Noinaj et al., 2014; Noinaj et al., 2013; Tomasek et al., 2020). Therefore,

429   the W-form hybrid-barrels probably represent a late intermediate stage that is unique to the

430   assembly of BamA. Because EspP follows the common architectural rules of most β-barrels, we

431   speculate that the majority of OMPs are folded through a late B-form hybrid-barrel stage before

432   β-signal exchange and β-seam closure causes the release of the fully folded β-barrel.

433   Our structural data also enable us to discriminate among a variety of models for BAM

434   function that have been previously proposed. We found that during its assembly by BAM, EspP

435   can associate with BamA to form structurally diverse hybrid-barrels and that in two

436   reconstructions EspP was observed in remarkable integrated open β-sheet conformations. Based

437   on these findings we propose a β-barrel folding model in which the open β-sheets close towards

438   BamA and then curl inwards to form a barrel-like structure at a late stage (Video S2). The

439   interface between BamAβ1 and the EspP β-signal does not change significantly between our ten

440   structures, yet the N-terminus of the EspP β-barrel undergoes enormous conformational changes.

441   These observations are fundamentally inconsistent with "threading" models which propose that

442   unfolded OMPs enter the BamA β-barrel lumen and form β-hairpins that are sequentially

443   integrated into the lipid bilayer through a "lateral gate" between BamA β1 and β16 (Horne et al.,

444   2020; Tomasek and Kahne, 2021). In contrast, our structures are consistent with our previous

445   study in which we showed that the interface between the BamA C-terminus and the EspP β-

446   barrel N-terminus is extremely dynamic but that the BamAβ1-β-signal interface is remarkably

447   stable during the hybrid-barrel stage *in vivo* (Doyle and Bernstein, 2019). Based on the results,

448   we proposed that the N-terminus of OMP β-barrels undergo a swinging action in the membrane

449   during their assembly. In light of our structural data, we speculate that 1) at early stages of

450   folding OMP β-signals are bound by BamAβ1, 2) this interaction templates the folding of the

451   adjacent OMP β-strands via β-augmentation (Remaut and Waksman, 2006) until an elongated β-

452   sheet is formed and 3) during the folding process the BamA β-barrel transitions from an inward-

453   open state to the outward-open state that we observed. The notion of sequential folding supports

454   the "BamA-elongation" model proposed by Schiffrin *et al* (2017), except that our OS-/IO-

455   substate structures raise the possibility that β-sheet elongation and OM integration occur

456   simultaneously. Independent of the role of BamA in OMP assembly, our finding that the

457   essential but enigmatic BamD subunit can interact with the turns of already integrated but

458   incompletely folded β-barrels is very striking. It is plausible that BamD supports the assembly

459   process by sensing the extent of substrate folding or by facilitating β-strand transfer.

460   Finally, our work yielded significant insights into the energetics of OMP assembly. First,

461   we obtained the first direct experimental evidence that the C-terminal side of the BamA β-barrel

462   can modify the thickness of the membrane and therefore lower the energy requirements for the

463   membrane integration of OMPs. Our results are in line with molecular dynamics simulations

464   (Liu and Gumbart, 2020; Noinaj et al., 2013), *in vitro* studies that indicate that membrane

465   thickness acts as a major barrier to OMP integration (Kleinschmidt and Tamm, 2002; Schiffrin et

466   al., 2017), and that membrane defects accelerate β-barrel folding (Danoff and Fleming, 2015).

467   Second, we obtained evidence that OMP assembly is not only driven by the free energy of

468 folding but that the late stages of OMP folding are accelerated by BAM harnessing OM tension

469 as a source of potential energy. Our experiments were inspired by an effort to explain the

470 purpose of the unprecedented structures of the deflected EspP open β-sheets bound to BamA in

471 an outward-open conformation. We proposed that the outward-open conformer of BamA holds

472 the β-signal of the folding OMP at an angle at which the intrinsic structure of the open β-sheet

473 state causes the hydrophobic transmembrane portions and aromatic girdles to deflect the OM.

474 However, the intrinsic tension in the OM would counter this deflection and thereby forces the β-

475 sheet to close into a β-barrel. Consistent with our model, we demonstrated that the rate of folding

476 after the formation of a hybrid-barrel can be transiently slowed by conditions that relaxed the

477 OM and can be accelerated when those conditions were reversed to increase the OM tension.

478 Furthermore, because the concentration of OMPs in the OM contributes to its rigidity (Lessen et

479 al., 2018; Rojas et al., 2018), it is plausible that the mysterious "OMP-islands" (pockets in the

480 bacterial OM with dense OMP packing and low diffusion) generate local zones of high OM

481 stiffness that promote the high β-barrel assembly activity attributed to them (Gunasinghe et al.,

482 2018; Rassam et al., 2015; Ursell et al., 2012). From a different perspective, a rigid membrane

483 might inhibit the integration of α-helical proteins which typically fold into fluid membranes.

484 Given that transmembrane β-barrel folding occurs in an environment that is devoid of known

485 external energy sources (e.g., ATP, GTP, or useful electrochemical gradients), the ability of

486 BAM to catalyze transmembrane β-barrel folding by a radically different mechanism that

487 harnesses the unusual properties of the OM might help to explain why the bacterial OM is

488 populated almost exclusively by β-barrel proteins.

22

489   **MATERIALS AND METHODS**

490   ***Plasmids, bacterial strains, and growth media***

491   The *E. coli* B strain BL21(DE3) (Invitrogen catalog number C600003) was used for all

492   experiments and *E. coli* K-12 strains XL1-Blue (Agilent catalog number 200236) or NEB5α

493   (NEB catalog number C2987H) were routinely used for cloning and mutagenesis. Strains were

494   grown in Lysogeny Broth (LB) (Miller or Lenox formulation as indicated) supplemented with

495   ampicillin (100 µg mL^{-1}) and/or trimethoprim (50 µg mL^{-1}) as necessary. Oligonucleotides and

496   plasmids used in this study are listed in Table S1. When necessary, BAM (^{His}BamABCDE) was

497   expressed from an IPTG inducible promoter in plasmid pMTD372 and $^{MBP-76}$EspP was expressed

498   from a *P*rhaB inducible promoter in plasmid pMTD607 (Doyle and Bernstein, 2019). Plasmids

499   expressing cysteine substitution mutant derivatives of pMTD372 and pMTD607 were generated

500   using the Q5 Site-Directed Mutagenesis Kit (NEB catalog number E0554S).

501

502   ***Purification of BAM-$^{MBP-76}$EspP native nanodiscs***

503   *E. coli* strain BL21(DE3) transformed with plasmids expressing ^{His}BamA$_{S425C}$BCDE and $^{MBP-}$

504   ^{76}EspP$_{S1299C}$ were grown overnight in LB (Miller) at 25 °C. Overnight cultures were then washed

505   and resuspended in fresh LB (1 culture volume) before inoculating 16 Thomson Ultra Yield

506   flasks (each containing 1 L of LB (Miller)) at a starting OD$_{600}$ of 0.05. Cultures were grown for 4

507   h (25 °C, 250 rpm), induced with 0.4 mM IPTG for 1 h, and then induced for a further 45 min

508   with 0.2% L-rhamnose. Each culture was pelleted (5,000 x *g*, 10 min, 4 °C), resuspended in 50

509   mL ice-cold phosphate buffered saline (PBS; 9 g L^{-1} NaCl, 0.144 g L^{-1} KH$_2$PO$_4$, 0.795 g L^{-1}

510   Na$_2$HPO$_4$, pH 7.4), and transferred to an Erlenmeyer flask on ice. Bacteria in each flask were

511   treated with a final concentration of 0.4 mM 4-DPS (4,4′-dipyridyl disulfide; a thiol-specific

512   disulfide oxidizing catalyst) for 30 min with orbital shaking at 100 rpm in packed ice, pelleted

513   (4,500 x g, 10 min, 4 °C), resuspended in 25 mL ice-cold PBS containing SigmaFast EDTA free

514   protease inhibitors (PI), and then frozen in liquid nitrogen. All 400 mL of harvested bacteria

515   were thawed and then lysed with a Constant Systems Cell Disruptor (15,000 psi, cooled to 5 °C).

516   Cell debris was removed (20,000 x g, 15 min, 4 °C) and then the lysate was ultracentrifuged

517   (194,903 x g, 2 h, 4 °C) to harvest membrane pellets. Using a Dounce homogenizer, membranes

518   were homogenized in 55 mL native-nanodisc buffer (3 % Xiran SL30010P20 (Orbiscope), 50

519   mM TrisHCl, 500 mM NaCl, 10 % glycerol, 1 mM EDTA, pH 8) containing freshly added PI

520   and incubated at 4 °C for 5 h with constant inversion. The solution was ultracentrifuged (265,455

521   x g, 40 min, 4 °C) and then the supernatant was collected and diluted 1:2 with a buffer (50 mM

522   TrisHCl, 500 mM NaCl, 10 % glycerol, pH 8 at 4 °C) containing freshly added PI. The diluted

523   protein solution was then incubated with 25 mL StrepTactin XT superflow resin (IBA GmbH) at

524   4 °C overnight with constant inversion. The protein-resin solution was then transferred to a

525   gravity column (all column steps mentioned hereafter were conducted at 4 °C) and the protein

526   flow-through was passed over the resin a second time. The resin was washed with 10 x 50 mL

527   TN buffer (50 mM TrisHCl, 500 mM NaCl, pH 8) at 4 °C before BAM-[MBP-76]EspP native

528   nanodiscs were eluted with 150 mL biotin buffer (50 mM biotin, 50 mM TrisHCl, 500 mM

529   NaCl, pH 8) at 4 °C. To concentrate and further purify the sample, imidazole (20 mM final) was

530   added to the eluted protein which was subsequently incubated with 5 mL NiNTA resin (Qiagen)

531   at 4 °C overnight with constant inversion. The protein solution was then transferred to a gravity

532   column and the protein flow-through was passed over the resin twice more. The resin was

533   washed with 3 x 10 mL of a buffer (20 mM imidazole, 50 mM TrisHCl, 500 mM NaCl pH 8) at

534   4 °C before BAM-[MBP-76]EspP native nanodiscs were eluted with 15 mL of elution buffer (500

535   mM imidazole, 50 mM TrisHCl, 150 mM NaCl pH 8) at 4 °C. The eluted protein was desalted

536   and exchanged into TN^{low} buffer (50 mM TrisHCl, 150 mM NaCl, pH 8 at 4 °C) using Sephadex

537   G-25 PD-10 desalting columns (Cytiva) following the manufacturers protocol before

538   concentrating to a volume of 20-50 µL using an Amicon Ultra 0.5 mL concentrator (10 kDa cut-

539   off). BAM-$^{MBP-76}$EspP native nanodiscs were used immediately in grid-preparations. For each

540   preparation, correct folding was confirmed by heat-modifiability/mobility-shift assays and

541   activity was assessed by *in vitro* assembly-restart assays (see below).

542

543   ***Cryo-EM sample preparation and imaging***

544   BAM-$^{MBP-76}$EspP native nanodiscs were diluted in TN^{low} buffer at a concentration of ~2 – 8 mg

545   L^{-1}, and 3 µL of sample was applied onto glow-discharged C-flat grids (EMS CF-1.2/1.3-4Au-

546   50) for 3 sec before plunge freezing in liquid ethane using a Leica EM Grid Plunger (Leica

547   Microsystems). Datasets were collected at the NIH Multi-Institute Cryo-EM Facility (MICEF)

548   using a Titan Krios G3 microscope (Thermo-Fisher) operating at 300 kV. During 4 collection

549   sessions (Figure S5, dataset 1) micrographs were collected at a magnification of 130,000x

550   (calibrated pixel size 0.5371 Å, nominal defocus range 0.6 to 1.8 µm, 40 frames, and 60 $e^-/Å^2$

551   electron exposure per movie) using a Gatan K2 Summit direct electron detection camera

552   equipped with a Gatan Quantum LS imaging energy filter with slit width set to 20 eV. After the

553   microscope was upgraded with a Gatan K3 camera an additional collection session (Figure S5,

554   dataset 2) was conducted at a magnification of 105,000x (calibrated pixel size 0.4281 Å, nominal

555   defocus range 0.6 to 1.8 µm, 23 frames, and 60 $e^-/Å^2$ electron exposure per movie).

556

557   ***Cryo-EM image processing***

558   Movie frames of BAM-$^{MBP-76}$EspP cryo-electron micrographs were motion corrected and dose-

559   weighted with MotionCor2 in RELION 3.1 (Zheng et al., 2017; Zivanov et al., 2018). CTF

560   estimation was determined in RELION 3.1 using Ctffind4 (Rohou and Grigorieff, 2015). Initial

561   particle picking was done with the Laplacian-of-Gaussian-based autopicking. Picked particles

562   were processed to generate an initial 3D reference for autopicking in RELION 3.1. A total of

563   25,393,510, particles, from dataset 1 collected on the K2 camera, and 9,873,900 particles, from

564   dataset 2 on the K3 camera, were picked. Following one round of 2D classification and three

565   rounds of 3D classification 3,996,756 particles from both datasets were merged with pixel size of

566   1.07 Å /pixel. Because we aimed to visualize intermediate folding states of EspP, we performed

567   focused classification 3D classification on the 3,996,756 million particles after signal subtraction

568   of heterogenous BamA P3, BamB, and BamD N-terminus components, which yielded a subset of

569   1,187,709 particles. These particles produced a 4.4 Å map using RELION 3.1. Following CTF

570   refinement and particle polishing, the 1,187,709 particles were processed by three strategies in

571   parallel using RELION 3.1 (Figure S5). Strategy 1 generated a 4.2 Å map after 3D refinement.

572   Strategy 2 used 3D classification of the 1,187,709 particles in RELION 3.1 to reveal six classes

573   of the BAM-$^{MBP-76}$EspP complex. Strategy 3 used focused classification and refinement after

574   signal subtraction of BamA P3, BamB, and BamD N-terminus revealed three folding states of

575   EspP. Particles from strategy 1, the six classes in strategy 2, and the 3 states in strategy 3 were

576   moved from the RELION 3.1 pipeline to cryoSPARC for further cryo-EM image processing

577   (Punjani et al., 2017; Punjani et al., 2020). Following pruning of the particle sets by rounds of

578   heterogenous refinement and final refinements, the following cryo-EM maps were obtained: (1)

579   a 3.6 Å map of BAM-$^{MBP-76}$EspP from strategy 1; (2) six cryo-EM maps capturing the motion in

580   the soluble subunits of BAM-$^{MBP-76}$EspP from strategy 2 [class 1 (4.5 Å), class 2 (4.3 Å), class 3

581   (4.2 Å), class 4 (4.3 Å), class 5 (4.3 Å), and class 6 (4.2 Å)]; (3) three cryo-EM maps following

582   focused classification/refinement of the substrate region produced the OS-state (4.3 Å), IO-state

583   (4.3 Å), and the B/CO-state (4.8 Å) stemming from strategy 3. Local resolution filtered maps

584   were produced in cryoSPARC.

585

586   ***Model building and refinement***

587   Initial fitting of BAM-$^{MBP-76}$EspP subunits into cryo-EM maps was done manually in UCSF

588   Chimera (Pettersen et al., 2004) using Bam complex subunits from PDB 5D0O (Gu et al., 2016),

589   EspP from PDB 2QOM and 3SLJ (Barnard et al., 2007; Barnard et al., 2012), and

590   lipopolysaccharide from 5W7B (Gorelik et al., 2018). For the high-resolution 3.6 Å map, manual

591   building/corrections of BamA subunits, EspP and LPS was done in Coot 0.9 and Isolde followed

592   by model refinement using Rosetta and real-space refinement in Phenix (Adams et al., 2010;

593   Croll, 2018; Emsley et al., 2010; Wang et al., 2016). The high-resolution atomic model derived

594   from the 3.6 Å map was used as a starting model for building models of the six classes (from

595   strategy 2) and the three focused states (from strategy 3). Because the substrate region in the

596   focused maps is observed at low resolution, some of the EspP β-barrel N-terminus was docked

597   into the map. The membrane interacting regions of EspP were better defined, could be identified

598   by the orientations of proteins in OPM server (Lomize et al., 2012), and modeled into the cryo-

599   EM map using Rosetta, Coot and Isolde (Croll, 2018; Emsley et al., 2010; Wang et al., 2016).

600   The cryo-EM data collection, final refinement, and validation statistics for the 10 atomic models

601   are presented in Table S2. Structural analysis, measurements and figures were prepared in

602   Chimera and ChimeraX (Pettersen et al., 2021).

603

604   *Data and code availability*

605   Structural data supporting findings in this study have been deposited in the Protein Data Bank

606   (PDB) and the Electron Microscopy Data Bank (EMDB). The accession codes of the cryo-EM

607   maps and accompanying atomic models have been provided for: (1) BAM-$^{MBP-76}$EspP *high-*

608   *resolution* (EMDB-xxxxx, PDB:xxx): (2) BAM-$^{MBP-76}$EspP *class 1* (EMDB-xxxxx, PDB:xxx):

609   (3) BAM-$^{MBP-76}$EspP *class 2* (EMDB-xxxxx, PDB:xxx): (4) BAM-$^{MBP-76}$EspP *class 3* (EMDB-

610   xxxxx, PDB:xxx): (5) BAM-$^{MBP-76}$EspP *class 4* (EMDB-xxxxx, PDB:xxx): (6) BAM-$^{MBP-76}$EspP

611   *class 5* (EMDB-xxxxx, PDB:xxx): (7) BAM-$^{MBP-76}$EspP *class 6* (EMDB-xxxxx, PDB:xxx): (8)

612   BAM-$^{MBP-76}$EspP *open-sheet EspP state* (EMDB-xxxxx, PDB:xxx): (9) BAM-$^{MBP-76}$EspP

613   *intermediate-open EspP state* (EMDB-xxxxx, PDB:xxx): (10) BAM-$^{MBP-76}$EspP *barrelized*

614   *EspP/ continuous open BamA state* (EMDB-xxxxx, PDB:xxx).

615

616   *In vivo disulfide-bond formation assay*

617   To observe site-specific interactions between BamD and the EspP β-barrel *in vivo*, disulfide-

618   bond formation assays were conducted essentially as described (Doyle and Bernstein, 2019,

619   2021). Briefly, strains containing appropriate plasmids were grown overnight from a single

620   colony in 10 mL LB (Miller) at 25 °C with orbital shaking (250 rpm). Cultures were pelleted

621   (3000 x g, 5 min, 4 °C), washed with 10 mL LB (Miller), and resuspended in 10 mL LB (Miller)

622   before inoculating 10 mL LB (Miller) subcultures at $OD_{600} = 0.05$. After cultures were grown for

623   4 h (25 °C, 250 rpm) to $OD_{600} \sim 0.4 - 0.6$, a final concentration of 0.4 mM IPTG was added to

624   induce expression of BAM for 1 h. Subsequently, a final concentration of 0.2% L-rhamnose was

625   added to induce expression of $^{MBP-76}$EspP for 45 min. 1 mL samples were aliquoted into tubes on

626   ice, pelleted (10,000 x g, 2 min, 4 °C), resuspended in 1 mL of ice-cold PBS, and incubated on

627   ice with 4-DPS at a concentration of 0.2 mM (or an equivalent volume of ethanol for mock

628   treatment controls). After 30 min, samples were pelleted (10,000 x g, 2 min, 4 °C) and

629   resuspended in 0.5 mL ice-cold PBS. Bacteria were then lysed, and proteins were precipitated by

630   adding a final concentration of 10% (v/v) trichloroacetic acid (TCA) and 4 mM

631   phenylmethanesulfonyl fluoride (PMSF) and incubating for 10 min on ice. The precipitated

632   proteins were pelleted (20,817 x g, 10 min, 4 °C), washed with 0.6 mL ice-cold acetone, re-

633   pelleted, and air-dried at 37 °C for 20 min. Proteins were resuspended in 2x SDS protein gel

634   loading solution (Quality Biological) in a volume normalized to an OD_{600} measurement recorded

635   immediately as subculture samples were taken (volume in µL = 200 x OD_{600}). Samples were

636   heated to 99 °C for 15 min and aliquots (5 µL) resolved by SDS-PAGE on 8 % – 16 % Tris-

637   glycine minigels (Invitrogen) (150 V, 1 h 47 min, room temperature) before being transferred to

638   nitrocellulose for immunoblot analysis.

639

640   ***Heat-modifiability/gel mobility-shift assay***

641   To observe the folded states of the BamA-EspP hybrid-barrel, purified BAM-[MBP-76]EspP native

642   nanodiscs were diluted 1:9 in ice-cold TN buffer before aliquots were further diluted 1:9 in

643   modified loading buffer (2x SDS protein gel loading solution serially diluted 1:1 with 20 %

644   glycerol twice and then 1:1 again with TN buffer for a final SDS concentration of 0.5%) on ice.

645   Aliquots were either heated to 99 °C for 10 min or retained on ice and proteins were immediately

646   resolved by cold-SDS-PAGE (gel tank in packed ice, running at 150 V, 4 °C cold room). Gels

647   were subsequently Coomassie Brilliant Blue (R-250) stained to detect proteins.

648

649   ***In vivo [MBP-76]EspP assembly-restart assays***

650   To monitor the final stages of assembly of EspP after the formation of a hybrid-barrel

651   intermediate with BamA, bacteria containing plasmids that express BAM and $^{MBP-76}$EspP were

652   cultured overnight from a single colony in 10 mL LB (Lenox) at 25 °C with orbital shaking (250

653   rpm). Cultures were pelleted (4,000 x g, 3 min, 4 °C), washed with LB (Lenox), and resuspended

654   in 10 mL LB (Lenox) before inoculating 10 mL LB (Lenox) subcultures at $OD_{600} = 0.05$. To

655   create a pool of molecules at a hybrid-barrel intermediate stage of assembly in bacteria,

656   subcultures were grown and the expression of BAM and $^{MBP-76}$EspP was induced as in the

657   disulfide-bond formation assays described above. Aliquots (1 mL samples) were then pelleted

658   (10,000 x g, 2 min, 20 °C), resuspended in equivalent volumes of either LB (Lenox) or LB

659   (Lenox) containing 0.8 M sorbitol (LB-Sorbitol), and pre-incubated in a Thermomixer

660   (Eppendorf) (20 °C, 350 rpm). After 5 min pre-incubation, 200 µg mL^{-1} PK (or an equivalent

661   volume of 50 mM TrisHCl pH 8 for mock-treated controls) was added and bacteria were

662   incubated (20 °C, 350 rpm) for 0, 2, 5, 10, and 20 min. For experiments requiring media

663   exchange from LB-Sorbitol, samples incubated with PK for 5 min were pelleted (15,000 x g, 20

664   s, 20 °C), resuspended in 1 mL of either LB (Lenox) or LB-Sorbitol (media pre-equilibrated to

665   20 °C), and further incubated (20 °C, 350 rpm) until 10 or 20 min after PK addition. For

666   experiments requiring disulfide-crosslinking, bacteria incubated with PK for 5 min were pelleted

667   (15,000 x g, 20 s, 4 °C), resuspended on ice in 1 mL ice-cold LB (Lenox) or LB-Sorbitol

668   (matching the previous incubation medium for each sample), and incubated on ice for 2 min in

669   the presence of 4-DPS (0.2 mM final concentration). To stop reactions at required time-points,

670   bacteria were pelleted (15,000 x g, 20 s, 4 °C), resuspended in 0.5 mL ice-cold LB (Lenox) or

671   LB-Sorbitol (matching the previous incubation medium for each sample), and TCA precipitated

672   as described above. Precipitated proteins were solubilized and resolved by SDS-PAGE as

673   described above.

674

675   ***Immunoblotting and image quantitation***

676   The iBlotII transfer device (Life Technologies) was routinely used to transfer protein gels to

677   nitrocellulose membranes. Immunoblotting buffer [Odyssey Blocking Buffer (Li-Cor) and PBS

678   (mixed together at a 1:1 ratio)] supplemented with 0.01 % Tween-20 was used for blocking steps

679   and as a diluent for primary and secondary antibodies. Monoclonal mouse anti-StrepII and anti-

680   His antibodies were obtained from QIAGEN (catalog number 34850) and Genscript (catalog

681   number A00186), respectively. Polyclonal rabbit anti-BamD and anti-EspP$_{\beta C}$ have been

682   described previously (Pavlova et al., 2013). Infra-red Goat anti-mouse Ig secondary antibodies

683   (anti-mouse 800CW IRDye, catalog number 926-32210) or anti-rabbit Ig (anti-rabbit 680LT

684   IRDye, catalog number 926-680210) were obtained from Li-Cor. Membranes were blocked

685   overnight, incubated with primary antibodies for 18 h, washed twice with PBS-T (PBS

686   supplemented with 0.01 % Tween-20), incubated for 2 h with secondary antibodies, and washed

687   twice with PBS-T and three times with PBS before air drying (37 °C, 20 min). Dried membranes

688   were scanned using maximum quality and resolution settings with an Amersham Typhoon 5

689   imager (GE Healthcare) outfitted with 785 nm and 685 nm lasers and IRlong 825BP30 and

690   IRShort 720BP20 filters. Within-lane pixel intensities were measured using Fiji software (v2.0.0-

691   rc-68/1.52 g) and used to calculate the fraction of the band of interest relative to other bands of

692   interest [e.g. for assembly restart assays, the fraction of folded EspP β-barrel was determined by

693   using the formula [folded EspP β-barrel/sum of EspP signals)].

694

703

AUTHOR CONTRIBUTIONS

704

705   The study was originally conceived by MTD and HDB, but all authors contributed to

706   experimental design. The experiments and data processing were conducted by MTD and JRJ.

707   The paper was written and edited by all authors. The project was supervised by JEH and HDB.

708

709   **FIGURES & LEGENDS**
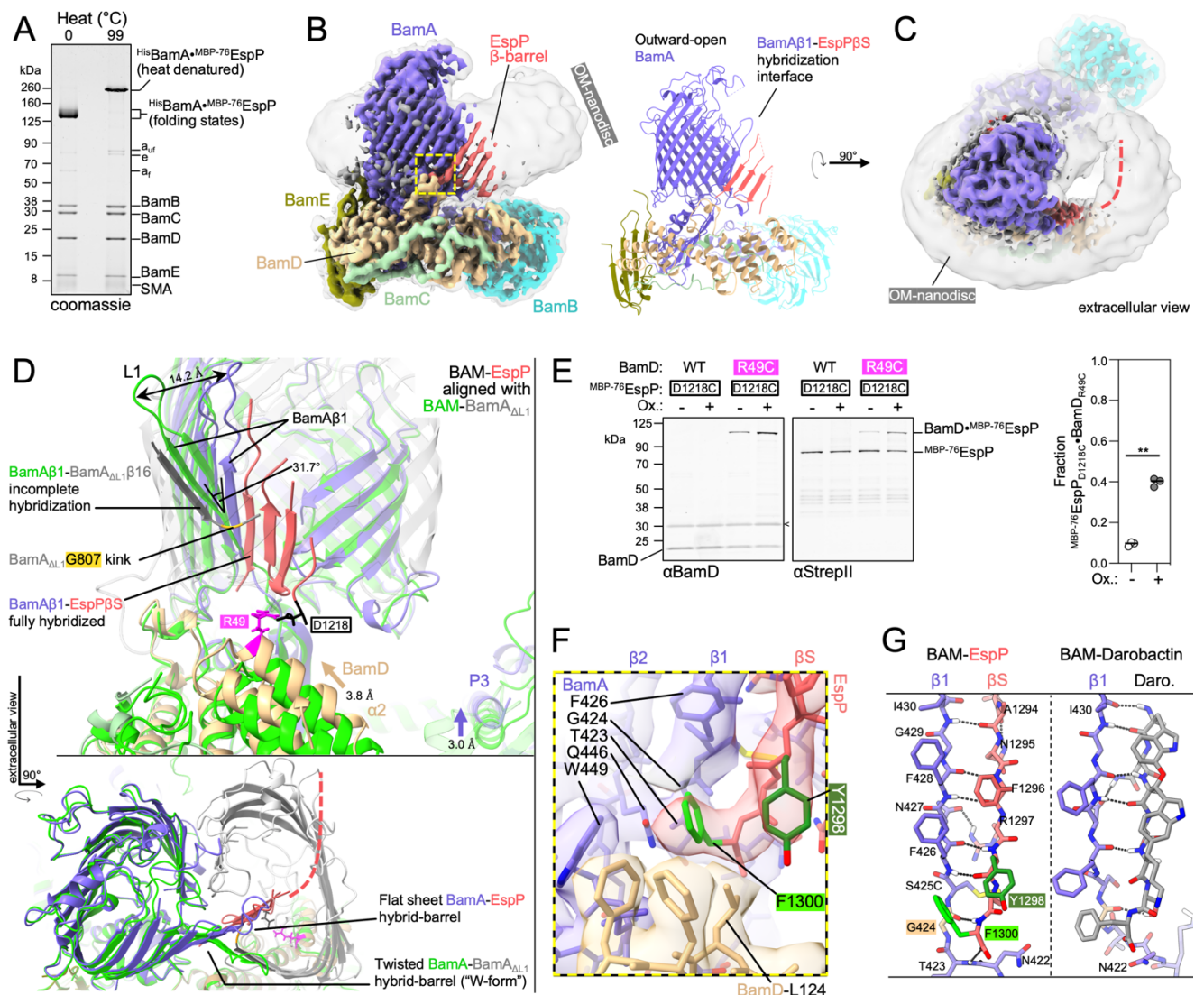
710

711   **Figure 1: BAM binds the conserved OMP β-signal to form a flat hybrid β-sheet in the OM.**

712   **(A)** Heat denatured (99 °C) or unheated BAM-$^{MBP-76}$EspP OM-nanodiscs were resolved by cold-

713   SDS-PAGE. BamA and $^{MBP-76}$EspP are disulfide-crosslinked (•) (via S425C and S1299C,

714   respectively). Unoxidized $^{MBP-76}$EspP (e), BamA folded (a_f) and unfolded (a_{uf}) species, and SMA

715   copolymers are indicated. **(B)** High-resolution cryo-EM map (left, 3.6 Å average) and model of

716   BAM-$^{MBP-76}$EspP (3.6 Å average). Map colored by subunit. Local resolution filtered map at a

717   lower threshold level (left, transparent grey) shows OM disc boundary. BamA is in an outward-

33

718   open conformation and hybridized to the EspP β-signal (βS) strand via BamA β-strand 1 (β1).

719   Yellow box shown in **F**. **(C)** Extracellular top view of map as in **B**. Dashed line indicates likely

720   location of remainder of EspP β-barrel. **(D)** Substrate-specific intermediate states and BAM

721   conformations during the assembly of EspP β-barrel and $BamA_{\Delta L1}$. Structure of BAM-$BamA_{\Delta L1}$

722   hybrid-barrel intermediate state in detergent (PBD 6V05) (BAM, green; $BamA_{\Delta L1}$, transparent

723   grey) is aligned with the BAM-$^{MBP-76}$EspP structure (subunit colors as in **C**). The noncanonical

724   final strand of $BamA_{\Delta L1}$ is not fully hybridized with Bamβ1 (kink at $BamA_{G807}$, yellow)

725   whereas the conserved EspP β-signal strand is fully hybridized with Bamβ1. A 31.7° difference

726   in Bamβ1 tilt angle [axis residues 427 – 434 alpha carbons (αC)] coincides with either "flat-

727   sheet" (BamA-EspP) or twisted "W-shaped" (BamA-$BamA_{\Delta L1}$) hybrid-barrel assembly

728   intermediates. BamA POTRA3 ("P3") and BamD α-helix 2 ("α2") are denoted. **(E)** *E. coli*

729   BL21(DE3) expressing ^{His}BamABCDE (or ^{His}BamABCD$_{R49C}$E) and $^{MBP-76}$EspP$_{D1218C}$ (residues

730   mutated to cysteine indicated in **D**) were mock treated (Ox. -) or treated with 4-DPS (Ox. +) and

731   BamD•$^{MBP-76}$EspP crosslinks were identified by double-immunoblotting with αBamD and

732   αStrepII (StrepII-tag at $^{MBP-76}$EspP N-terminus) antibodies (n = 3). Non-specific band is denoted

733   (<). The graph (right) shows the fraction of crosslinked BamD•$^{MBP-76}$EspP [line at median, two-

734   tailed paired t-test: $P = 0.0019$ (**)]. **(F)** β-signal terminal residue binding pocket (magnified

735   yellow box in **B**). Highly conserved Y(-3, dark green) and F(-1, light green) β-signal residues are

736   indicated. **(G)** Comparison of Bamβ1-EspP β-signal strand and Bamβ1-darobactin (PDB

737   7NRI) interactions. In both cases F(-1) is positioned over the space created by $BamA_{G424}$ (tan).

738   Dotted lines denote H-bonds.

739
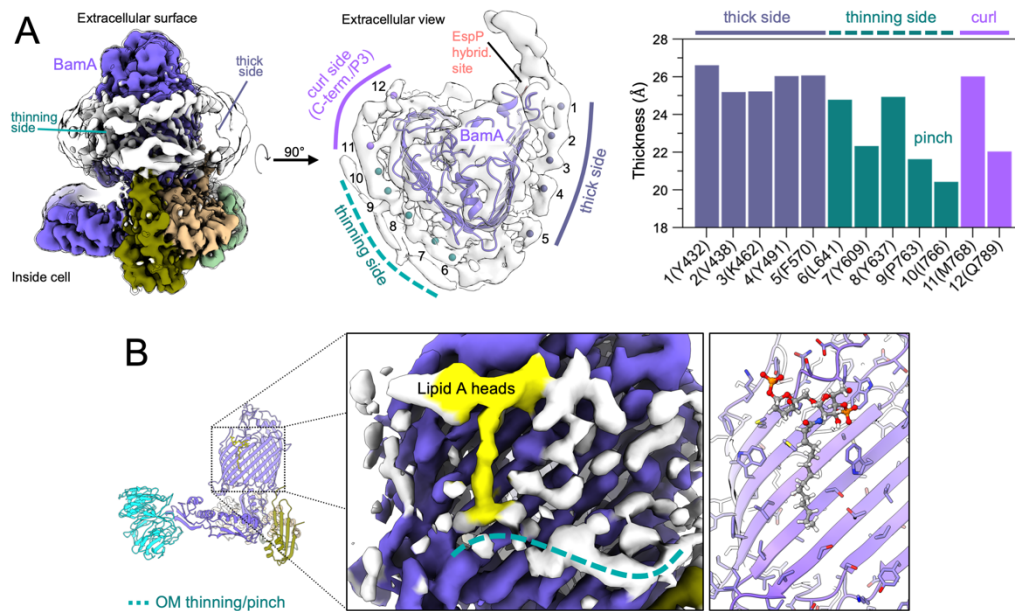
Figure 2: OM thinning and lipid/LPS ordering during OMP folding. (A) Left, side view of BAM-MBP-76EspP showing both thin and thick membrane sides around BamA [local resolution filtered map to showing protein (colored) and membrane (white) features and at a lower threshold (clear) to show OM-disc boundary]. Middle, extracellular view of map with measurement marker positions (circles) indicated. Repeated pattern in the OM-disc indicative of outer leaflet interfacial lipid A head groups. Right, thickness measurements of membrane density surrounding the BamA β-barrel at indicated positions (residues close to outer leaflet markers in brackets). **(B)** BAM-MBP-76EspP map shows density consistent with a lipid A head groups and a stabilized acyl chain (yellow) (modeled on right) on the thinning side of the BamA β-barrel (teal dashed line).

750

751
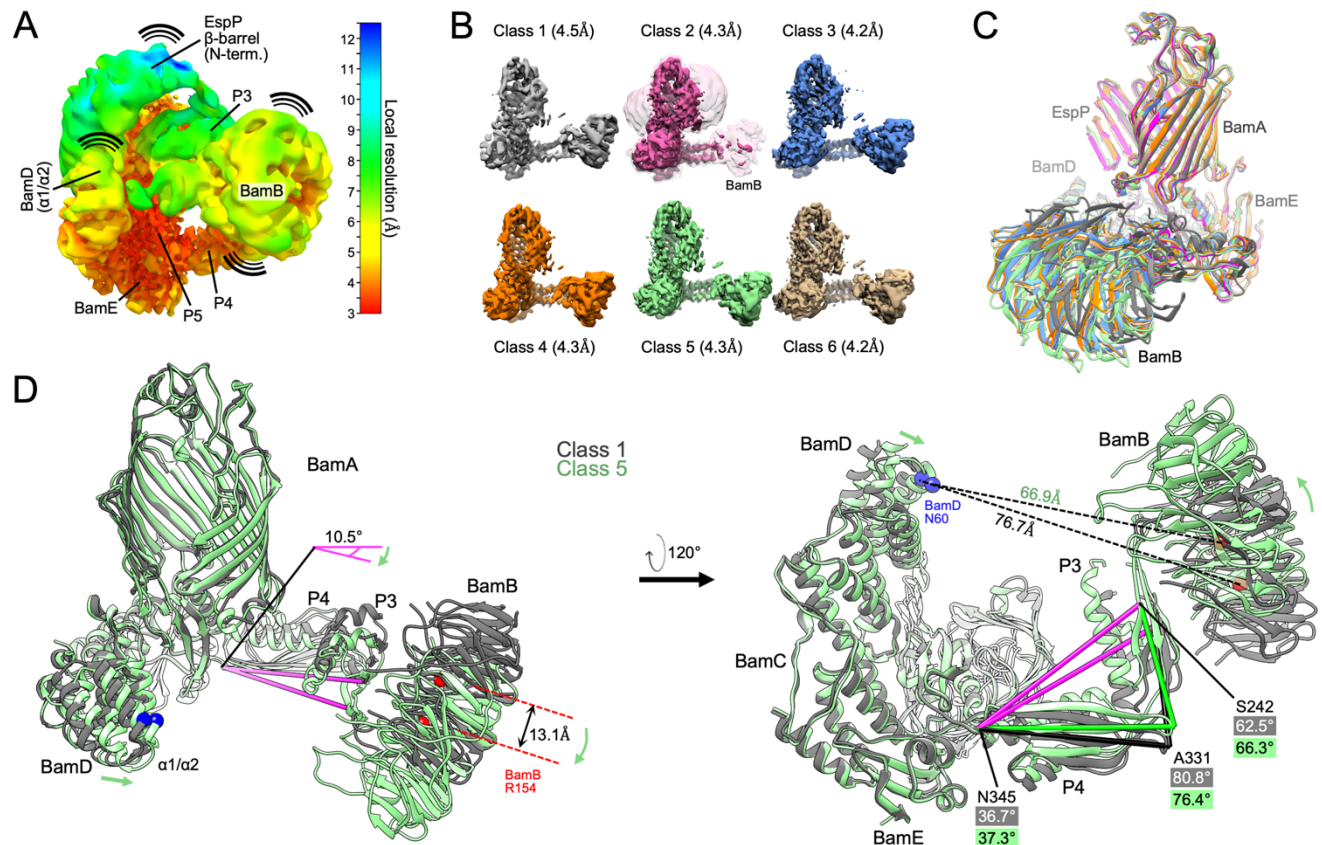
**Figure 3: Conformational changes of BAM periplasmic components during OMP folding.**

(A) The BAM-[MBP-76]EspP high-resolution map (shown in Figure 1B) filtered and colored by

local resolution. Low resolution components [e.g. EspP β-barrel N-terminus, BamB, and

POTRA3 (P3)] are conformationally dynamic. High-resolution components (e.g. BamE and P5

are conformationally stable. **(B)** Conformationally diverse cryo-EM maps of BAM-[MBP-76]EspP.

Maps filtered by local resolution. Class 2 is shown at a lower threshold level (clear pink) to show

BamB **(C)** Models of BAM-[MBP-76]EspP Classes 1 – 6 were aligned (based on BamA P5 residues

Y348 – R421). View shows large conformational variability in BamB positioning. Colors as in

B. **(D)** Classes 1 and 5 aligned as in **C**. Conformational changes are depicted by green arrows.

Axis (pink) from BamA S242 (P3) to N345 (hinge region between P4 & P5) α-carbons flexes by

10.5° between classes. Changes in the angles between S242, A331, and N345 also shows flexing

between P3 & P4 between classes.

36
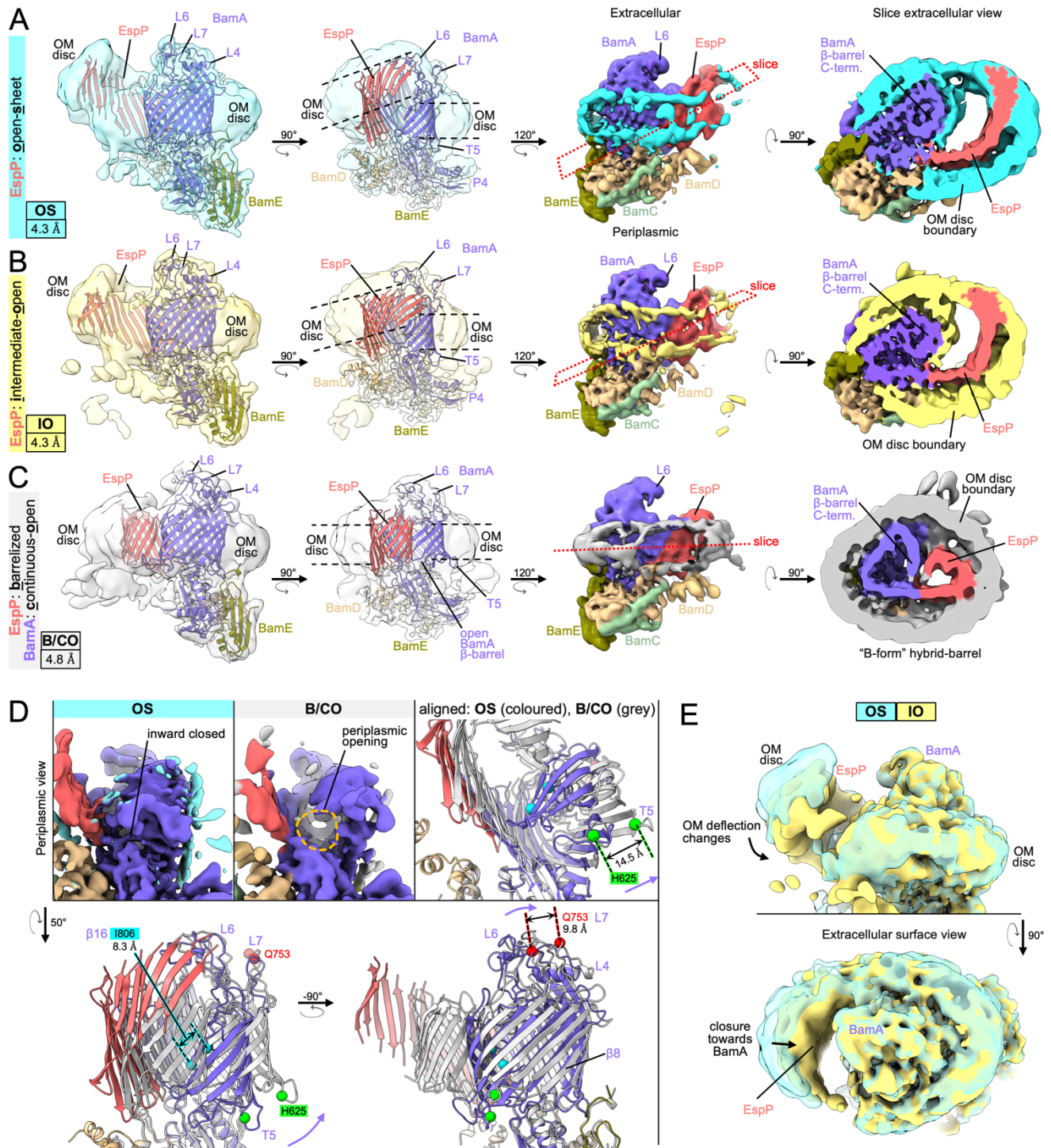
764

765 **Figure 4: Focused classification reveals a continuous-open BamA β-barrel and multiple**

766 **hybrid-barrel substates during EspP folding. (A-C)** Focused classification and refinements on

767 particles with subtracted signals of dynamic periplasmic components (BamD N-term., P3, and

768 BamB) identified three distinct BamA-EspP hybrid-barrel conformations: EspP "open-sheet"

769 (OS, panel **A**, OM-disc in cyan), EspP "intermediate-open" (IO, panel **B**, OM-disc in yellow),

770 and EspP "barrelized" / BamA "continuous-open" (B/CO, panel **C**, OM-disc in light gray). Map

771 resolutions are quoted at bottom left. Dashed lines in mid-left views indicate in-plane or

772 deflected bilayer angles. Right views, maps are colored by subunit. Far-right shows slices across

773 the BamA-EspP hybrid-barrels (slice planes depicted mid-right) with expanded hybrid-barrels

774 for OS and IO, and a "B-shaped" hybrid-barrel for the B/CO state. Maps are filtered by local

775 resolution. **(D)** Identification of a novel BamA conformation during OMP assembly. Compared

776 to the OS class (and all other reconstructions in this work) the B/CO class exhibits the BamA β-

777 barrel in an expanded conformation similar to outward-open conformations but with a

778 periplasmic opening (compare maps top left and middle, periplasmic view). In top-right and

779 bottom panels, models of OS and B/CO states are aligned (on P5 residues Y348 – R421)

780 showing that the C-terminal half of the BamA β-barrel both expands and shifts towards the cell

781 surface through changes beginning at strand β8. The expansion also coincides with extracellular

782 loops (L4, 6, and 7) moving away from the hybridization interface. Differences in selected

783 residue αC positions in turn 5 (T5, H625), L7 (Q753), and β16 (I806) between OS and B/CO

784 states are denoted. **(E)** Overlay of OS and IO maps (filtered by local resolution) shows changes

785 in the degree of OM-bilayer deflection and degree of closure in the EspP β-sheet region.

786

787
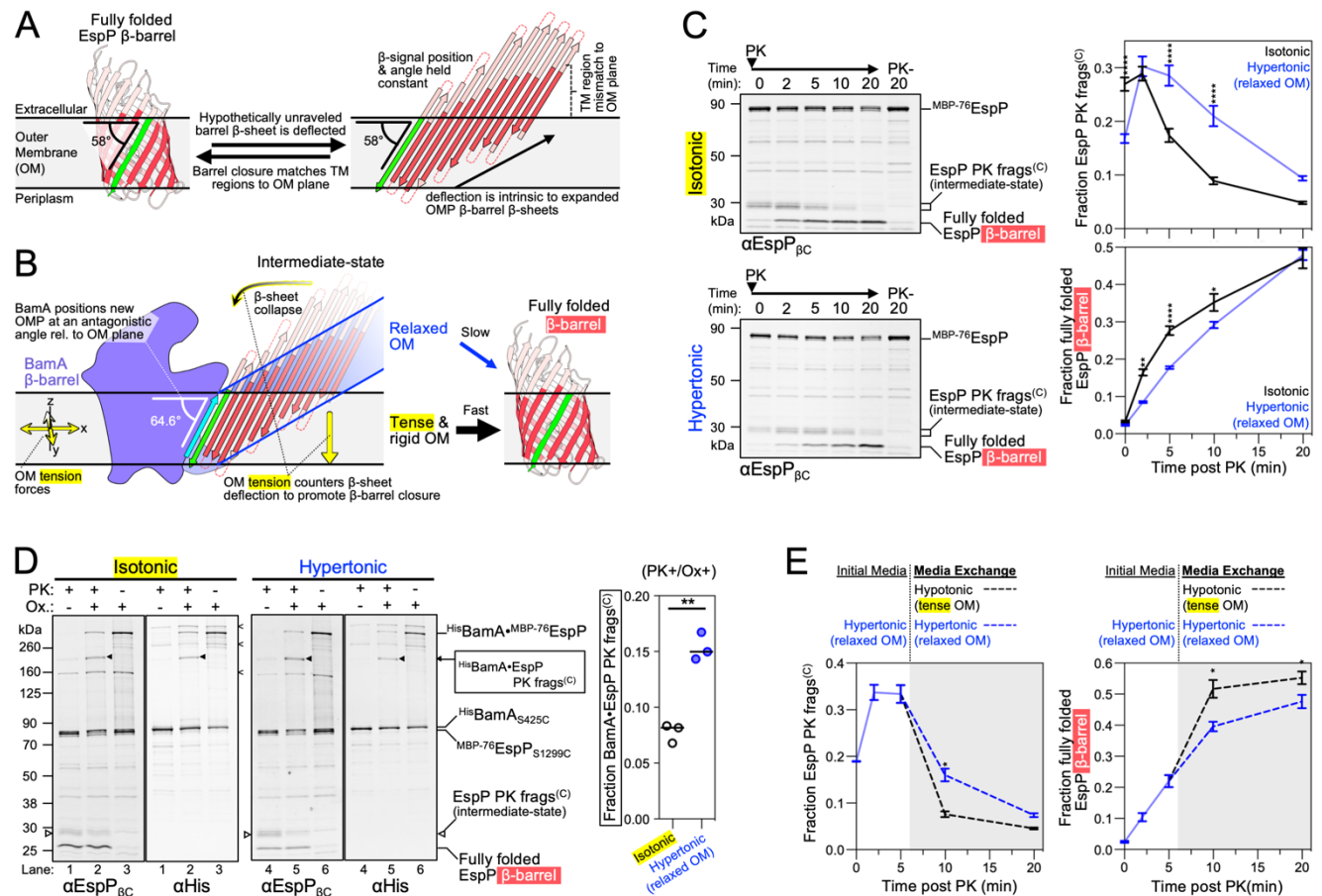
Figure 5: OM tension accelerates transmembrane β-barrel folding. (A) Hypothetically

unraveled EspP β-barrel with the position of the conserved β-signal strand (green) held constant

to its angular membrane orientation when fully folded (58° for EspP, membrane plane calculated

using OPM server) (Lomize et al., 2012) showing intrinsic mismatch between the membrane

plane and the transmembrane portion of β-strands (red). Depicted loops and turns are not drawn

to-scale. **(B)** EspP β-sheet as in **A** except model depicted with experimentally determined angle

(using the BAM-[MBP-76]EspP high resolution structure) of EspP β-signal relative to the membrane

when hybridized to BamAβ1 (cyan). The model predicts that the intrinsic tension forces of the

rigid OM of Gram-negative bacteria aids β-barrel folding by countering the intrinsic deflection

of an incompletely folded expanded β-sheet. **(C)** *E. coli* BL21(DE3) expressing [His]BamABCDE

and [MBP-76]EspP were suspended in LB (isotonic control) or LB-sorbitol (hypertonic) to generate

799   cells with a relaxed OM. β-barrel folding was restarted from the hybrid-barrel stage by adding

800   PK to release a C-terminal EspP fragment (frags$^{(C)}$). Fragment conversion to a completely folded

801   β-barrel after PK addition was monitored by immunoblotting using an antiserum generated

802   against the C-terminus of EspP (αEspP$_{βC}$). Left, representative blots. Right, mean fraction of the

803   EspP PK fragment (top) or converted into a folded β-barrel (bottom) (±SEM, n = 4). **(D)** *E. coli*

804   BL21(DE3) expressing ^{His}BamA$_{S425C}$BCDE and $^{MBP-76}$EspP$_{S1299C}$ were grown and treated as in **C**

805   except that samples at 5 min post PK were mock treated (Ox. -) or treated with 4-DPS (Ox. +)

806   and ^{His}BamA•$^{MBP-76}$EspP crosslinks were identified by double-immunoblotting with αEspP$_{βC}$ and

807   αHis antibodies (n = 3). Non-specific crosslinks are denoted (<). Right, fraction of crosslinked

808   BamA•$^{MBP-76}$EspP C-terminal PK fragment out of all bands detected with αEspP$_{βC}$ [line at

809   median, two-tailed paired t-test: $P = 0.0038$ (**)]. **(E)** Bacteria were grown, suspended in LB-

810   sorbitol, and treated with PK as in **C** except that after 5 min the media was exchanged for either

811   LB-sorbitol (hypertonic) or LB (hypotonic) (gray plot area). Plots are mean fraction (±SEM, n =

812   3). For **C** and **E**, 2-way repeated measures ANOVA (Šídák's tests) were performed *p < 0.05,

813   **p < 0.01, and ****p < 0.0001.

814

REFERENCES

815

816 Adams, P.D., Afonine, P.V., Bunkóczi, G., Chen, V.B., Davis, I.W., Echols, N., Headd, J.J., Hung, L.W., Kapral,
817 G.J., Grosse-Kunstleve, R.W., *et al.* (2010). PHENIX: a comprehensive Python-based system for macromolecular
818 structure solution. Acta Crystallogr D Biol Crystallogr *66*, 213-221. 10.1107/S0907444909052925.
819
820 Anwari, K., Webb, C.T., Poggio, S., Perry, A.J., Belousoff, M., Celik, N., Ramm, G., Lovering, A., Sockett, R.E.,
821 Smit, J., *et al.* (2012). The evolution of new lipoprotein subunits of the bacterial outer membrane BAM complex.
822 Mol Microbiol *84*, 832-844. 10.1111/j.1365-2958.2012.08059.x.
823
824 Barnard, T.J., Dautin, N., Lukacik, P., Bernstein, H.D., and Buchanan, S.K. (2007). Autotransporter structure
825 reveals intra-barrel cleavage followed by conformational changes. Nat Struct Mol Biol *14*, 1214-1220.
826 10.1038/nsmb1322.
827
828 Barnard, T.J., Gumbart, J., Peterson, J.H., Noinaj, N., Easley, N.C., Dautin, N., Kuszak, A.J., Tajkhorshid, E.,
829 Bernstein, H.D., and Buchanan, S.K. (2012). Molecular basis for the activation of a catalytic asparagine residue in a
830 self-cleaving bacterial autotransporter. J Mol Biol *415*, 128-142. 10.1016/j.jmb.2011.10.049.
831
832 Croll, T.I. (2018). ISOLDE: a physically realistic environment for model building into low-resolution electron-
833 density maps. Acta Crystallogr D Struct Biol *74*, 519-530. 10.1107/S2059798318002425.
834
835 Danoff, E.J., and Fleming, K.G. (2015). Membrane defects accelerate outer membrane beta-barrel protein folding.
836 Biochemistry *54*, 97-99. 10.1021/bi501443p.
837
838 Dautin, N., Barnard, T.J., Anderson, D.E., and Bernstein, H.D. (2007). Cleavage of a bacterial autotransporter by an
839 evolutionarily convergent autocatalytic mechanism. EMBO J *26*, 1942-1952. 10.1038/sj.emboj.7601638.
840
841 Doerner, P.A., and Sousa, M.C. (2017). Extreme Dynamics in the BamA beta-Barrel Seam. Biochemistry *56*, 3142-
842 3149. 10.1021/acs.biochem.7b00281.
843
844 Doyle, M.T., and Bernstein, H.D. (2019). Bacterial outer membrane proteins assemble via asymmetric interactions
845 with the BamA beta-barrel. Nat Commun *10*, 3358. 10.1038/s41467-019-11230-9.
846
847 Doyle, M.T., and Bernstein, H.D. (2021). BamA forms a translocation channel for polypeptide export across the
848 bacterial outer membrane. Mol Cell *81*, 2000-2012 e2003. 10.1016/j.molcel.2021.02.023.
849
850 Emsley, P., Lohkamp, B., Scott, W.G., and Cowtan, K. (2010). Features and development of Coot. Acta Crystallogr
851 D Biol Crystallogr *66*, 486-501. 10.1107/S0907444910007493.
852
853 Franklin, M.W., Nepomnyachyi, S., Feehan, R., Ben-Tal, N., Kolodny, R., and Slusky, J.S. (2018). Evolutionary
854 pathways of repeat protein topology in bacterial outer membrane proteins. Elife *7*. 10.7554/eLife.40308.
855
856 Gessmann, D., Chung, Y.H., Danoff, E.J., Plummer, A.M., Sandlin, C.W., Zaccai, N.R., and Fleming, K.G. (2014).
857 Outer membrane beta-barrel protein folding is physically controlled by periplasmic lipid head groups and BamA.
858 Proc Natl Acad Sci U S A *111*, 5878-5883. 10.1073/pnas.1322473111.
859
860 Gorelik, A., Illes, K., and Nagar, B. (2018). Crystal structure of the mammalian lipopolysaccharide detoxifier. Proc
861 Natl Acad Sci U S A *115*, E896-E905. 10.1073/pnas.1719834115.
862
863 Gruss, F., Zahringer, F., Jakob, R.P., Burmann, B.M., Hiller, S., and Maier, T. (2013). The structural basis of
864 autotransporter translocation by TamA. Nat Struct Mol Biol *20*, 1318-1320. 10.1038/nsmb.2689.
865
866 Gu, Y., Li, H., Dong, H., Zeng, Y., Zhang, Z., Paterson, N.G., Stansfeld, P.J., Wang, Z., Zhang, Y., Wang, W., *et al.*
867 (2016). Structural basis of outer membrane protein insertion by the BAM complex. Nature *531*, 64-69.
868 10.1038/nature17199.

869

870 Gunasinghe, S.D., Shiota, T., Stubenrauch, C.J., Schulze, K.E., Webb, C.T., Fulcher, A.J., Dunstan, R.A., Hay, I.D.,
871 Naderer, T., Whelan, D.R., *et al.* (2018). The WD40 Protein BamB Mediates Coupling of BAM Complexes into
872 Assembly Precincts in the Bacterial Outer Membrane. Cell Rep *23*, 2782-2794. 10.1016/j.celrep.2018.04.093.
873

874 Hagan, C.L., Wzorek, J.S., and Kahne, D. (2015). Inhibition of the beta-barrel assembly machine by a peptide that
875 binds BamD. Proc Natl Acad Sci U S A *112*, 2011-2016. 10.1073/pnas.1415955112.
876

877 Han, L., Zheng, J., Wang, Y., Yang, X., Liu, Y., Sun, C., Cao, B., Zhou, H., Ni, D., Lou, J., *et al.* (2016). Structure
878 of the BAM complex and its implications for biogenesis of outer-membrane proteins. Nat Struct Mol Biol *23*, 192-
879 196. 10.1038/nsmb.3181.
880

881 Hart, E.M., Gupta, M., Wuhr, M., and Silhavy, T.J. (2020). The gain-of-function allele bamA E470K bypasses the
882 essential requirement for BamD in beta-barrel outer membrane protein assembly. Proc Natl Acad Sci U S A *117*,
883 18737-18743. 10.1073/pnas.2007696117.
884

885 Hart, E.M., and Silhavy, T.J. (2020). Functions of the BamBCDE Lipoproteins Revealed by Bypass Mutations in
886 BamA. J Bacteriol *202*. 10.1128/JB.00401-20.
887

888 Heinz, E., and Lithgow, T. (2014). A comprehensive analysis of the Omp85/TpsB protein superfamily structural
889 diversity, taxonomic occurrence, and evolution. Front Microbiol *5*, 370. 10.3389/fmicb.2014.00370.
890

891 Heinz, E., Selkrig, J., Belousoff, M.J., and Lithgow, T. (2015). Evolution of the Translocation and Assembly
892 Module (TAM). Genome Biol Evol *7*, 1628-1643. 10.1093/gbe/evv097.
893

894 Horne, J.E., Brockwell, D.J., and Radford, S.E. (2020). Role of the lipid bilayer in outer membrane protein folding
895 in Gram negative bacteria. J Biol Chem. 10.1074/jbc.REV120.011473.
896

897 Iadanza, M.G., Higgins, A.J., Schiffrin, B., Calabrese, A.N., Brockwell, D.J., Ashcroft, A.E., Radford, S.E., and
898 Ranson, N.A. (2016). Lateral opening in the intact beta-barrel assembly machinery captured by cryo-EM. Nat
899 Commun *7*, 12865. 10.1038/ncomms12865.
900

901 Iadanza, M.G., Schiffrin, B., White, P., Watson, M.A., Horne, J.E., Higgins, A.J., Calabrese, A.N., Brockwell, D.J.,
902 Tuma, R., Kalli, A.C., *et al.* (2020). Distortion of the bilayer and dynamics of the BAM complex in lipid nanodiscs.
903 Commun Biol *3*, 766. 10.1038/s42003-020-01419-w.
904

905 Ieva, R., and Bernstein, H.D. (2009). Interaction of an autotransporter passenger domain with BamA during its
906 translocation across the bacterial outer membrane. Proc Natl Acad Sci U S A *106*, 19120-19125.
907 10.1073/pnas.0907912106.
908

909 Ieva, R., Tian, P., Peterson, J.H., and Bernstein, H.D. (2011). Sequential and spatially restricted interactions of
910 assembly factors with an autotransporter beta domain. Proc Natl Acad Sci U S A *108*, E383-391.
911 10.1073/pnas.1103827108.
912

913 Imai, Y., Meyer, K.J., Iinishi, A., Favre-Godal, Q., Green, R., Manuse, S., Caboni, M., Mori, M., Niles, S.,
914 Ghiglieri, M., *et al.* (2019). A new antibiotic selectively kills Gram-negative pathogens. Nature *576*, 459-464.
915 10.1038/s41586-019-1791-1.
916

917 Jaroslawski, S., Duquesne, K., Sturgis, J.N., and Scheuring, S. (2009). High-resolution architecture of the outer
918 membrane of the Gram-negative bacteria Roseobacter denitrificans. Mol Microbiol *74*, 1211-1222. 10.1111/j.1365-
919 2958.2009.06926.x.
920

921 Kaur, H., Jakob, R.P., Marzinek, J.K., Green, R., Imai, Y., Bolla, J.R., Agustoni, E., Robinson, C.V., Bond, P.J.,
922 Lewis, K., *et al.* (2021). The antibiotic darobactin mimics a beta-strand to inhibit outer membrane insertase. Nature
923 *593*, 125-129. 10.1038/s41586-021-03455-w.
924

925 Kleinschmidt, J.H., and Tamm, L.K. (2002). Secondary and tertiary structure formation of the beta-barrel membrane
926 protein OmpA is synchronized and depends on membrane thickness. Journal of Molecular Biology *324*, 319-330.
927 10.1016/S0022-2836(02)01071-9.
928
929 Kozjak, V., Wiedemann, N., Milenkovic, D., Lohaus, C., Meyer, H.E., Guiard, B., Meisinger, C., and Pfanner, N.
930 (2003). An essential role of Sam50 in the protein sorting and assembly machinery of the mitochondrial outer
931 membrane. J Biol Chem *278*, 48520-48523. 10.1074/jbc.C300442200.
932
933 Lauber, F., Deme, J.C., Lea, S.M., and Berks, B.C. (2018). Type 9 secretion system structures reveal a new protein
934 transport mechanism. Nature *564*, 77-82. 10.1038/s41586-018-0693-y.
935
936 Lee, J., Sutterlin, H.A., Wzorek, J.S., Mandler, M.D., Hagan, C.L., Grabowicz, M., Tomasek, D., May, M.D., Hart,
937 E.M., Silhavy, T.J.*, et al.* (2018). Substrate binding to BamD triggers a conformational change in BamA to control
938 membrane insertion. Proc Natl Acad Sci U S A *115*, 2359-2364. 10.1073/pnas.1711727115.
939
940 Lee, S.C., Knowles, T.J., Postis, V.L., Jamshad, M., Parslow, R.A., Lin, Y.P., Goldman, A., Sridhar, P., Overduin,
941 M., Muench, S.P.*, et al.* (2016). A method for detergent-free isolation of membrane proteins in their local lipid
942 environment. Nat Protoc *11*, 1149-1162. 10.1038/nprot.2016.070.
943
944 Lessen, H.J., Fleming, P.J., Fleming, K.G., and Sodt, A.J. (2018). Building Blocks of the Outer Membrane:
945 Calculating a General Elastic Energy Model for beta-Barrel Membrane Proteins. J Chem Theory Comput *14*, 4487-
946 4497. 10.1021/acs.jctc.8b00377.
947
948 Leyton, D.L., Johnson, M.D., Thapa, R., Huysmans, G.H., Dunstan, R.A., Celik, N., Shen, H.H., Loo, D., Belousoff,
949 M.J., Purcell, A.W.*, et al.* (2014). A mortise-tenon joint in the transmembrane domain modulates autotransporter
950 assembly into bacterial outer membranes. Nat Commun *5*, 4239. 10.1038/ncomms5239.
951
952 Liu, J., and Gumbart, J.C. (2020). Membrane thinning and lateral gating are consistent features of BamA across
953 multiple species. PLoS Comput Biol *16*, e1008355. 10.1371/journal.pcbi.1008355.
954
955 Lomize, A.L., Pogozheva, I.D., and Mosberg, H.I. (2011). Anisotropic solvent model of the lipid bilayer. 2.
956 Energetics of insertion of small molecules, peptides, and proteins in membranes. J Chem Inf Model *51*, 930-946.
957 10.1021/ci200020k.
958
959 Lomize, M.A., Pogozheva, I.D., Joo, H., Mosberg, H.I., and Lomize, A.L. (2012). OPM database and PPM web
960 server: resources for positioning of proteins in membranes. Nucleic Acids Res *40*, D370-376. 10.1093/nar/gkr703.
961
962 Lundquist, K., Bakelar, J., Noinaj, N., and Gumbart, J.C. (2018). C-terminal kink formation is required for lateral
963 gating in BamA. Proc Natl Acad Sci U S A *115*, E7942-E7949. 10.1073/pnas.1722530115.
964
965 Noinaj, N., Kuszak, A.J., Balusek, C., Gumbart, J.C., and Buchanan, S.K. (2014). Lateral opening and exit pore
966 formation are required for BamA function. Structure *22*, 1055-1062. 10.1016/j.str.2014.05.008.
967
968 Noinaj, N., Kuszak, A.J., and Buchanan, S.K. (2015). Heat Modifiability of Outer Membrane Proteins from Gram-
969 Negative Bacteria. Methods Mol Biol *1329*, 51-56. 10.1007/978-1-4939-2871-2_4.
970
971 Noinaj, N., Kuszak, A.J., Gumbart, J.C., Lukacik, P., Chang, H., Easley, N.C., Lithgow, T., and Buchanan, S.K.
972 (2013). Structural insight into the biogenesis of beta-barrel membrane proteins. Nature *501*, 385-390.
973 10.1038/nature12521.
974
975 Patel, R., Hsu, S.C., Bedard, J., Inoue, K., and Jarvis, P. (2008). The Omp85-related chloroplast outer envelope
976 protein OEP80 is essential for viability in Arabidopsis. Plant Physiol *148*, 235-245. 10.1104/pp.108.122754.
977
978 Pavlova, O., Peterson, J.H., Ieva, R., and Bernstein, H.D. (2013). Mechanistic link between beta barrel assembly and
979 the initiation of autotransporter secretion. Proc Natl Acad Sci U S A *110*, E938-947. 10.1073/pnas.1219076110.
980

43

981   Pettersen, E.F., Goddard, T.D., Huang, C.C., Couch, G.S., Greenblatt, D.M., Meng, E.C., and Ferrin, T.E. (2004).
982   UCSF Chimera--a visualization system for exploratory research and analysis. J Comput Chem *25*, 1605-1612.
983   10.1002/jcc.20084.
984
985   Pettersen, E.F., Goddard, T.D., Huang, C.C., Meng, E.C., Couch, G.S., Croll, T.I., Morris, J.H., and Ferrin, T.E.
986   (2021). UCSF ChimeraX: Structure visualization for researchers, educators, and developers. Protein Sci *30*, 70-82.
987   10.1002/pro.3943.
988
989   Prinz, W.A., and Hinshaw, J.E. (2009). Membrane-bending proteins. Crit Rev Biochem Mol Biol *44*, 278-291.
990   10.1080/10409230903183472.
991
992   Punjani, A., Rubinstein, J.L., Fleet, D.J., and Brubaker, M.A. (2017). cryoSPARC: algorithms for rapid
993   unsupervised cryo-EM structure determination. Nat Methods *14*, 290-296. 10.1038/nmeth.4169.
994
995   Punjani, A., Zhang, H., and Fleet, D.J. (2020). Non-uniform refinement: adaptive regularization improves single-
996   particle cryo-EM reconstruction. Nat Methods *17*, 1214-1221. 10.1038/s41592-020-00990-8.
997
998   Rassam, P., Copeland, N.A., Birkholz, O., Toth, C., Chavent, M., Duncan, A.L., Cross, S.J., Housden, N.G.,
999   Kaminska, R., Seger, U.*, et al.* (2015). Supramolecular assemblies underpin turnover of outer membrane proteins in
1000 bacteria. Nature *523*, 333-336. 10.1038/nature14461.
1001
1002 Remaut, H., and Waksman, G. (2006). Protein-protein interaction through beta-strand addition. Trends Biochem Sci
1003 *31*, 436-444. 10.1016/j.tibs.2006.06.007.
1004
1005 Rohou, A., and Grigorieff, N. (2015). CTFFIND4: Fast and accurate defocus estimation from electron micrographs.
1006 J Struct Biol *192*, 216-221. 10.1016/j.jsb.2015.08.008.
1007
1008 Rojas, E.R., Billings, G., Odermatt, P.D., Auer, G.K., Zhu, L., Miguel, A., Chang, F., Weibel, D.B., Theriot, J.A.,
1009 and Huang, K.C. (2018). The outer membrane is an essential load-bearing element in Gram-negative bacteria.
1010 Nature *559*, 617-621. 10.1038/s41586-018-0344-3.
1011
1012 Rossiter, A.E., Leyton, D.L., Tveen-Jensen, K., Browning, D.F., Sevastsyanovich, Y., Knowles, T.J., Nichols, K.B.,
1013 Cunningham, A.F., Overduin, M., Schembri, M.A.*, et al.* (2011). The essential beta-barrel assembly machinery
1014 complex components BamD and BamA are required for autotransporter biogenesis. J Bacteriol *193*, 4250-4253.
1015 10.1128/JB.00192-11.
1016
1017 Schiffrin, B., Calabrese, A.N., Higgins, A.J., Humes, J.R., Ashcroft, A.E., Kalli, A.C., Brockwell, D.J., and Radford,
1018 S.E. (2017). Effects of Periplasmic Chaperones and Membrane Thickness on BamA-Catalyzed Outer-Membrane
1019 Protein Folding. J Mol Biol *429*, 3776-3792. 10.1016/j.jmb.2017.09.008.
1020
1021 Schulz, G.E. (2000). beta-Barrel membrane proteins. Curr Opin Struct Biol *10*, 443-447. 10.1016/s0959-
1022 440x(00)00120-2.
1023
1024 Struyve, M., Moons, M., and Tommassen, J. (1991). Carboxy-Terminal Phenylalanine Is Essential for the Correct
1025 Assembly of a Bacterial Outer-Membrane Protein. Journal of Molecular Biology *218*, 141-148. Doi 10.1016/0022-
1026 2836(91)90880-F.
1027
1028 Sun, C., Benlekbir, S., Venkatakrishnan, P., Wang, Y., Hong, S., Hosler, J., Tajkhorshid, E., Rubinstein, J.L., and
1029 Gennis, R.B. (2018). Structure of the alternative complex III in a supercomplex with cytochrome oxidase. Nature
1030 *557*, 123-126. 10.1038/s41586-018-0061-y.
1031
1032 Tomasek, D., and Kahne, D. (2021). The assembly of beta-barrel outer membrane proteins. Curr Opin Microbiol *60*,
1033 16-23. 10.1016/j.mib.2021.01.009.
1034
1035 Tomasek, D., Rawson, S., Lee, J., Wzorek, J.S., Harrison, S.C., Li, Z., and Kahne, D. (2020). Structure of a nascent
1036 membrane protein as it folds on the BAM complex. Nature. 10.1038/s41586-020-2370-1.

1037
1038 Ursell, T.S., Trepagnier, E.H., Huang, K.C., and Theriot, J.A. (2012). Analysis of surface protein expression reveals
1039 the growth pattern of the gram-negative outer membrane. PLoS Comput Biol *8*, e1002680.
1040 10.1371/journal.pcbi.1002680.
1041
1042 Voulhoux, R., Bos, M.P., Geurtsen, J., Mols, M., and Tommassen, J. (2003). Role of a highly conserved bacterial
1043 protein in outer membrane protein assembly. Science *299*, 262-265. 10.1126/science.1078973.
1044
1045 Wang, R.Y., Song, Y., Barad, B.A., Cheng, Y., Fraser, J.S., and DiMaio, F. (2016). Automated structure refinement
1046 of macromolecular assemblies from cryo-EM maps using Rosetta. Elife *5*. 10.7554/eLife.17219.
1047
1048 Wang, X., Peterson, J.H., and Bernstein, H.D. (2021). Bacterial Outer Membrane Proteins Are Targeted to the Bam
1049 Complex by Two Parallel Mechanisms. mBio *12*. 10.1128/mBio.00597-21.
1050
1051 Weiss, M.S., Wacker, T., Weckesser, J., Welte, W., and Schulz, G.E. (1990). The three-dimensional structure of
1052 porin from Rhodobacter capsulatus at 3 A resolution. FEBS Lett *267*, 268-272. 10.1016/0014-5793(90)80942-c.
1053
1054 White, P., Haysom, S.F., Iadanza, M.G., Higgins, A.J., Machin, J.M., Whitehouse, J.M., Horne, J.E., Schiffrin, B.,
1055 Carpenter-Platt, C., Calabrese, A.N.*, et al.* (2021). The role of membrane destabilisation and protein dynamics in
1056 BAM catalysed OMP folding. Nat Commun *12*, 4174. 10.1038/s41467-021-24432-x.
1057
1058 Wu, E.L., Fleming, P.J., Yeom, M.S., Widmalm, G., Klauda, J.B., Fleming, K.G., and Im, W. (2014). E. coli outer
1059 membrane and interactions with OmpLA. Biophys J *106*, 2493-2502. 10.1016/j.bpj.2014.04.024.
1060
1061 Wu, T., Malinverni, J., Ruiz, N., Kim, S., Silhavy, T.J., and Kahne, D. (2005). Identification of a multicomponent
1062 complex required for outer membrane biogenesis in Escherichia coli. Cell *121*, 235-245. 10.1016/j.cell.2005.02.015.
1063
1064 Zheng, S.Q., Palovcak, E., Armache, J.P., Verba, K.A., Cheng, Y., and Agard, D.A. (2017). MotionCor2:
1065 anisotropic correction of beam-induced motion for improved cryo-electron microscopy. Nat Methods *14*, 331-332.
1066 10.1038/nmeth.4193.
1067
1068 Zivanov, J., Nakane, T., Forsberg, B.O., Kimanius, D., Hagen, W.J., Lindahl, E., and Scheres, S.H. (2018). New
1069 tools for automated high-resolution cryo-EM structure determination in RELION-3. Elife *7*. 10.7554/eLife.42166.
1070
1071